Research Paper
Computational Methods for Differential Equations
http://cmde.tabrizu.ac.ir
Vol. *, No. *, *, pp. 1-32
DOI:10.22034/cmde.2026.67348.3202

Numerical simulations of tangent hyperbolic fluid flow is performed on the upper horizontal surface of a paraboloid of revolution by Keller Box method

Atif Ali Zafar[1,*], **Habiba Niaz**[1], **Hadia Parveen**[2]

[1]Department of Mathematics, Capital University of Science and Technology Islamabad, Pakistan.

[2]Department of Mathematics, National University of Modern Languages, Islamabad, Pakistan.

Abstract

This study examines tangent hyperbolic fluid flow over a paraboloid surface in the presence of quartic autocatalytic chemical reactions between homogeneous and heterogeneous phases. The model incorporates thermal radiation, spatially varying heat generation, Brownian motion, thermophoresis, and an external magnetic field. The governing equations are reduced to nonlinear ODEs and solved using the Keller Box Method, effectively capturing the shear-thinning nature of the fluid. Results reveal that radiation and heat generation strongly influence temperature distribution, while Brownian and thermophoretic effects modify flow and thermal fields. Furthermore, increasing magnetic strength and the Weissenberg number enhances the Nusselt number, indicating improved heat transfer through magnetic effects and fluid elasticity.

Keywords. Paraboloid of revolution, Quartic autocatalysis, Tangent hyperbolic, MHD flow, Brownian motion, Thermophoresis.
2010 Mathematics Subject Classification. 65L05, 34K06, 34K28.

1. Introduction

The tangent hyperbolic fluid is a non-Newtonian fluid model that effectively characterizes both shear-thinning and shear-thickening behaviors. Unlike Newtonian fluids, its viscosity varies with the rate of shear strain, enabling it to adapt under different flow conditions. This property makes the model especially useful in simulating complex fluids encountered in real-world scenarios such as polymer solutions, biofluids, paints, and coatings. Its versatility renders it indispensable in various industrial applications, particularly in coating processes, polymer extrusion, biomedical engineering, and thermal management systems, where precise control over fluid behavior is critical. A key aspect of this research area is the theoretical analysis of fluid properties. In this regard, the work by [2] provides an important contribution by examining the regularity of weak solutions to fluid flows.

The tangent hyperbolic fluid model has proven effective in capturing diverse magneto-thermo-fluidic phenomena in porous and non-porous domains. The study by [25] delves into the numerical simulation of unsteady squeezing nanofluid and heat flow, providing a relevant precedent for the numerical approach taken in this paper. Nasir et al. [27] explored solutal–thermal stratification effects on tangent hyperbolic Buongiorno nanofluid flow over a porous stretching sheet, utilizing the Homotopy Analysis Method (HAM) to reveal velocity suppression with increasing Weissenberg number, and thermal amplification via elevated Biot number. Asogwa et al. [7] analyzed electro-magneto-hydrodynamic flow incorporating volumetric heating, Arrhenius kinetics, and cross-diffusion, offering valuable insights into reactive flow systems. Gaffar et al. [12] assessed the thermomagnetic responses of a micropolar tangent hyperbolic fluid over a non-isothermal conical surface, highlighting the impact of micro-rotation and anisotropic heating. Moltot et al. [26] investigated the unsteady magnetohydrodynamic (MHD) flow of a tangent hyperbolic ternary hybrid nanofluid through a Darcy–Forchheimer porous medium, accounting for variable thermal conductivity—an important consideration in enhanced geothermal systems.

Received: 17 May 2025; Accepted: 14 April 2026.
∗Corresponding author. Email: zafaratifali@gmail.com; zafaratifali56@gmail.com.

Chemical reactions—classified as homogeneous or heterogeneous based on phase uniformity—constitute the core of diverse catalytic systems [5]. Kim [16] revisited Lotka's autocatalytic models, highlighting nonlinear feedback in chemical oscillations. Hu and Sapre [13] emphasized the significance of isothermal catalysis in biochemical and petrochemical processes. Animasaun et al. [6] modeled viscoelastic flows governed by coupled autocatalytic and first-order kinetics, noting the cubic model's limitations at elevated wall-catalyst concentrations. AlBaidani et al. [4] linked rheological shifts in Maxwell nanofluids to reaction-modulated Deborah numbers. Waini et al. [31] showed that hybrid nanofluids, through reactive species, intensify shear and solutal effects while suppressing thermal transport.

Thermophoresis, critical in applications like reactor safety and aerosol filtration, alongside Brownian motion—first noted by Ingenhousz and later formalized by Einstein and Wiener—profoundly shapes particle transport. Their combined effect has garnered interest in MHD transport studies. Matin et al. [24] analyzed these phenomena in nanofluid flow between co-rotating cylinders, while Malvandi et al. [23] assessed heat transfer during film boiling. Hussain et al. [14] investigated pseudo-plastic nanofluids, revealing non-Newtonian responses. Shafey et al. [30] and Obalalu et al. [28] extended the analysis to Newtonian and reactive fluids near stretched and vertically translating cylinders. In a related study, [9] explores a numerical study of bioconvection and the Cattaneo-Christov heat flux model in MHD Maxwell nanofluid flow, offering a comparative perspective on similar complex fluid behaviors.

In addition to traditional numerical schemes, wavelet-based methods have recently emerged as efficient tools for solving nonlinear transport problems. Haar and orthogonal wavelet approaches, for instance, have been successfully applied to nanofluid heat transfer, porous media flows, and unsteady squeezing flow configurations [18, 29]. These studies demonstrate the capability of wavelets to handle complex thermal and fluid systems with good accuracy and computational efficiency. However, their use in boundary-layer problems involving non-Newtonian fluids and multiphysics interactions is still very limited. This gap reinforces the relevance of employing the Keller Box Method in the present work, as it provides a more stable and well-established framework for analyzing nonlinear boundary-layer dynamics.

To the best of our knowledge, this is the first comprehensive study that combines a paraboloid geometry, tangent hyperbolic non-Newtonian fluid model, and multiphysics transport phenomena within the Keller Box framework. This unique integration sets a new benchmark for the analysis of nonlinear boundary-layer flows, offering insights directly relevant to advanced engineering and industrial applications. The work is anchored in key research questions, offering a novel and integrative framework.

- How does increasing the magnetic parameter (M) enhance heat transfer efficiency in electrically conducting fluids, and what role do secondary flow structures play in this enhancement?
- In what ways does fluid elasticity, characterized by the Weissenberg number (We), contribute to enhanced convective heat transfer, and how does it alter boundary layer dynamics?
- How do buoyancy-driven flows, represented by the thermal Grashof number (Gr), influence the development of horizontal velocity profiles and surface-driven convection?
- How does thermal radiation (Rd) influence temperature distribution in a radiative heat transfer system, and why does it lead to lower overall temperature profiles?
- How does the Brownian motion parameter (Nb) simultaneously enhance thermal conductivity and reduce local heat transfer at the surface in fluids?
- How do mass transport parameters such as the Schmidt number (Sc_a) and thermophoresis parameter (Nt) control concentration and temperature profiles in chemically reacting fluid systems?

The rest of this paper is structured as follows. Section 1 introduces the study and includes several supporting subsections: the Novelty of the Present Work highlights the originality of the research; Flow Assumptions describe the theoretical basis and simplifications; the Motivation and Research Gap outlines deficiencies in prior studies; Real-Life Applications connect the model with practical systems; and the Advantages and Limitations of the Proposed Scheme assess the Keller Box Method against other numerical techniques.

Section 2 provides an overview, historical background, and numerical methodology of the Keller Box Method, highlighting its accuracy and adaptability. Section 3 presents the mathematical modeling of the tangent hyperbolic fluid flow with the inclusion of homogeneous–heterogeneous reactions, nonlinear radiation, and transport effects. In Section 4, the governing equations are non-dimensionalized and transformed into a system of nonlinear ordinary differential

equations. Section 5 offers a comprehensive discussion of the Keller Box Method's significance and applications, while Section 6 details the solution methodology adopted in this work. Section 7 presents numerical results and physical interpretations, whereas Section 8 provides validation and comparison with earlier studies to ensure the accuracy of the present findings. Section 9 presents graphical simulations and a detailed discussion of the different profiles. Finally, Section 10 concludes the paper with key outcomes and potential directions for future research.

In order to strengthen the quality and originality of the present work, several key aspects have been highlighted through dedicated subsections. First, the *Novelty of the Present Work* is emphasized, where the unique combination of a paraboloid geometry, tangent hyperbolic non-Newtonian model, and advanced physical effects is discussed. This is followed by *Flow Assumptions*, clearly outlining the theoretical basis and simplifications adopted to ensure a tractable yet realistic formulation. The *Motivation and Research Gap* subsection situates the study within the broader context of existing literature, identifying unexplored areas that justify the present investigation. To bridge theory with practice, a separate discussion on *Real-Life Applications* is provided, demonstrating how the proposed model is relevant to industrial, biomedical, and technological systems. Finally, the *Advantages and Limitations of the Proposed Scheme* are critically evaluated, with a comparative table underscoring the strengths of the Keller Box Method against established approaches. Collectively, these subsections ensure clarity, depth, and relevance, presenting a rigorous framework that enhances the impact of this research.

1.1. **Novelty of the Present Work.** The originality of this work lies in its integrated treatment of a highly complex fluid dynamic system. It is the first study to analyze tangent hyperbolic fluid flow over a paraboloid of revolution while simultaneously accounting for magnetic field effects, quartic autocatalytic reactions, nonlinear thermal radiation, Brownian motion, thermophoresis, and spatially varying heat generation. Unlike conventional approaches, the present model captures the combined influence of these mechanisms within a single framework, offering a more realistic representation of engineering and industrial processes. Moreover, the application of the Keller Box Method to this multiphysics configuration is itself a novel contribution, as this scheme has not been systematically employed for curved geometries with such intricate couplings. Together, the unique geometry, comprehensive physical modeling, and robust numerical methodology establish the study as a distinctive contribution, providing new insights and benchmarks for future research in non-Newtonian magneto-thermo-fluid dynamics.

1.2. **Flow Assumptions.** The mathematical formulation of the problem is based on the following assumptions:

- The fluid is incompressible and follows the tangent hyperbolic non-Newtonian model, accounting for shear-thinning behavior.
- The flow is steady, laminar, and two-dimensional, developing along the surface of a paraboloid of revolution.
- A uniform magnetic field is applied normal to the flow direction, while induced magnetic effects are neglected due to low magnetic Reynolds number.
- The boundary layer approximation is employed, assuming that gradients in the normal direction dominate over streamwise variations.
- Thermal radiation is included using the Rosseland diffusion approximation.
- Internal heat generation/absorption is considered as a spatially varying function.
- Homogeneous (bulk) and heterogeneous (surface) quartic autocatalytic reactions are incorporated in the concentration field.
- Brownian motion and thermophoresis effects are included to capture nanoscale particle dynamics.
- Fluid properties are assumed constant, except for density variations in the buoyancy term (Boussinesq approximation).
- Viscous dissipation and Joule heating are neglected.

1.3. **Motivation and Research Gap.** Although non-Newtonian models such as the tangent hyperbolic fluid have been widely investigated, most existing studies are restricted to simplified geometries such as flat plates, cylinders, or channels. In practical situations, however, fluid flow frequently occurs over curved surfaces, where curvature significantly alters the boundary-layer structure and heat transfer characteristics. Despite this importance, systematic research on curved geometries remains limited.

TABLE 1. Comparison of the Keller Box Method with established numerical schemes.

Feature	Keller Box Method (KBM)	Shooting Method (SM)	bvp4c
Stability	Implicit scheme, unconditionally stable for stiff nonlinear problems	Sensitive to initial guesses; may diverge	Generally stable but may fail for strongly nonlinear systems
Accuracy	Second-order accurate in both space and time	High accuracy possible, but dependent on guess quality	Adaptive mesh ensures good accuracy
Boundary Conditions	Handles complex, mixed, or nonlinear BCs effectively	Struggles with complex/mixed boundary conditions	Can handle most BCs, but less flexible for coupled nonlinear BCs
Computational Cost	Efficient block-tridiagonal solver; moderate effort required	Lower cost per iteration, but may require many iterations	Efficient due to built-in optimization
Implementation Effort	Requires system reduction, discretization, and LU factorization	Relatively simple to implement	Easy to use (built-in function)
Best Use Cases	Nonlinear boundary-layer flows, MHD, heat and mass transfer problems	Simple BVPs with well-posed initial conditions	General-purpose BVP solver for moderate complexity

Another limitation in the literature is the tendency to treat physical effects in isolation. For instance, some works emphasize magnetic fields, others focus on chemical reactions or thermal radiation, while very few attempt to study their combined influence. In real-world systems, these mechanisms rarely act independently, and their interactions may produce unexpected nonlinear responses. This lack of integrative studies highlights the need for a unified framework that can capture multiphysics coupling in a realistic manner.

From a numerical perspective, the situation is equally restrictive. Many studies rely on shooting methods, Runge–Kutta schemes, or built-in solvers such as BVP4c. While these approaches are useful for moderately nonlinear problems, they often become unstable or inefficient when applied to strongly coupled systems involving multiple transport processes. In contrast, the Keller Box Method (KBM) is well-known for its robustness, stability, and suitability for nonlinear boundary-layer flows. Yet, its potential has not been fully utilized for complex configurations such as paraboloid geometries with multiphysics effects.

Taken together, these gaps reveal a clear opportunity for advancing current understanding: a comprehensive study of tangent hyperbolic fluid flow over a curved configuration, incorporating multiple interacting physical processes and solved with the Keller Box Method. Such an effort not only strengthens the theoretical modeling of non-Newtonian flows but also enhances the reliability and applicability of numerical simulations to engineering and industrial systems.

1.4. **Real-Life Applications.** The present investigation is not purely theoretical but carries practical relevance in several advanced engineering and industrial systems. The tangent hyperbolic fluid model is widely used to describe shear-thinning fluids such as polymer solutions, paints, and biofluids, which appear in coating processes, extrusion operations, and biomedical transport. The paraboloid surface considered in this study is representative of curved geometries encountered in aerodynamic nose-cones, reflector antennas, catalytic reactors, and thermal management devices, where curvature plays a key role in flow and heat transfer.

The inclusion of a quartic autocatalytic reaction reflects realistic scenarios in catalytic chemical processes, fuel cells, and biochemical systems, where both homogeneous and heterogeneous reactions occur simultaneously. Similarly, the effects of Brownian motion and thermophoresis are important in nanofluid applications, such as targeted drug delivery, microchannel cooling of electronic components, and aerosol filtration technologies. Moreover, the role of an external magnetic field is particularly relevant in magnetohydrodynamic generators, plasma reactors, and cooling systems in nuclear and metallurgical industries.

Thus, the present study provides insights that are directly transferable to real-world problems where non-Newtonian behavior, reactive transport, and coupled thermal phenomena over curved geometries are of critical importance.

1.5. **Advantages and Limitations of the Proposed Scheme.** The Keller Box Method (KBM) offers several advantages compared with more conventional numerical schemes such as the shooting method, Runge–Kutta approaches, or MATLAB's BVP solvers. Its implicit formulation ensures strong numerical stability, particularly for stiff and highly nonlinear systems, while the block-tridiagonal structure of the resulting algebraic system allows efficient computation even with fine grid resolutions. Unlike shooting methods, which can suffer from divergence when initial guesses are poor, KBM converges reliably over a broad parameter space. Moreover, it handles complex boundary conditions—such as coupled, nonlinear, or mixed types—with greater flexibility than explicit schemes.

On the other hand, KBM requires a more elaborate implementation, involving reduction to first-order systems, linearization, and matrix factorization at each iteration. This increases the programming effort compared with readily available solvers like BVP4c. Additionally, for problems with very high dimensionality or ill-conditioned systems, orthogonal factorizations or spectral methods may achieve better numerical stability. Nevertheless, for boundary-layer flows with moderate computational demands, the Keller Box Method strikes an effective balance between accuracy, robustness, and efficiency, validating its relevance in the present study. For clarity, some of these advantages and limitations are summarized in Table 1 below.

2. Introduction to the Keller Box Method

2.1. **Overview.** The Keller Box method is one of the most reliable and widely applied numerical techniques for solving boundary layer-type problems in fluid mechanics, heat transfer, and other transport phenomena. Its popularity stems from its robustness, accuracy, and efficiency when dealing with nonlinear and coupled systems that often pose challenges to traditional numerical schemes. By combining methodological rigor with computational stability, the Keller Box method provides an effective framework for analyzing a broad spectrum of engineering and scientific problems.

2.2. **Historical Background.** The origins of the Keller Box method can be traced back to the early 1970s, when Herbert B. Keller introduced the scheme to address the limitations of existing approaches for boundary layer analysis. Many classical numerical techniques at the time, such as the shooting method and explicit Runge–Kutta schemes, were prone to instability and required restrictive assumptions. Keller's innovation was to design an implicit finite-difference formulation that systematically reduced higher-order nonlinear differential equations into a system of first-order equations, discretized them through a box-type scheme, and solved the resulting system iteratively using Newton's method. This development marked a breakthrough in numerical analysis, as it enabled researchers to solve stiff and nonlinear equations with second-order accuracy and strong stability, establishing the method as a cornerstone in computational mathematics.

2.3. **Numerical Methodology.** From a methodological perspective, the Keller Box scheme follows a structured sequence. First, the governing higher-order differential equations are transformed into an equivalent system of first-order equations. Next, these are discretized over a computational grid using a box scheme that guarantees second-order accuracy. The resulting nonlinear algebraic system is then linearized and solved through Newton's method, while block elimination is employed to simplify computations. This structured procedure ensures stability and efficiency, allowing the method to handle nonlinearities, coupled systems, and complex boundary conditions more effectively than many alternative numerical approaches.

2.4. **Significance and Applications.** The significance of the Keller Box method lies in both its accuracy and adaptability. Researchers have successfully applied it to a wide variety of physical problems, including viscous flows, magnetohydrodynamic flows, porous media transport, and heat and mass transfer processes. Its ability to produce reliable solutions with comparatively fewer computational resources highlights its practical importance in modern research. Unlike conventional methods, which may face difficulties in dealing with strongly nonlinear or stiff systems, the Keller Box approach provides a consistent and flexible framework that remains relevant even with the increasing complexity of present-day models.

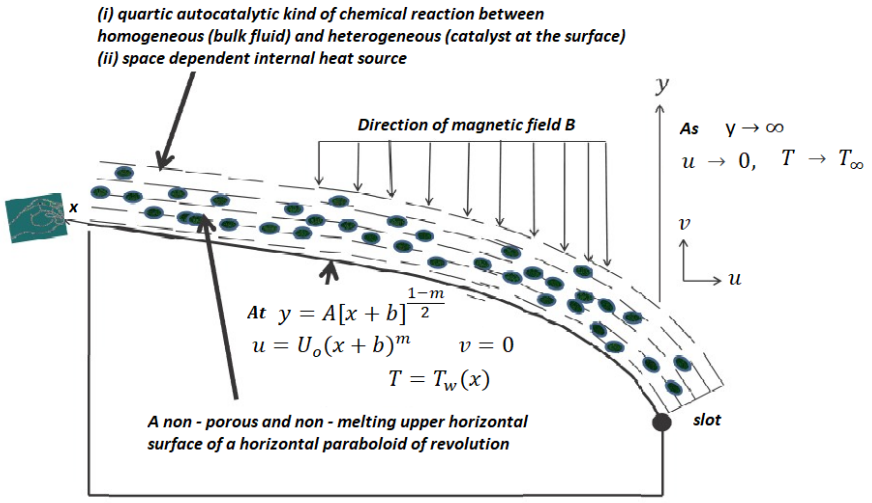

FIGURE 1. The coordinate system and arrangement for the scenario $m < 1$ from left to right across a surface with varying thickness.

2.5. **Motivation for the Present Study.** In view of these strengths, the Keller Box method has been chosen for the present study. Many engineering and scientific problems involve highly nonlinear governing equations with coupled boundary conditions that cannot be solved efficiently using simpler schemes. The Keller Box method not only provides the required stability and accuracy but also ensures that the solutions obtained are robust across a wide parameter space. Its continued application in contemporary research underscores its reliability and relevance. Therefore, adopting this method ensures that the present work is supported by a strong and well-established numerical foundation, providing both clarity in theoretical formulation and motivation for practical implementation.

3. MATHEMATICAL MODELING

The present study rigorously examines the steady, laminar, and two-dimensional flow dynamics of a tangent hyperbolic fluid over a continuously deforming paraboloidal stretching surface, accounting for spatially varying internal heat generation alongside nonlinear thermal radiation effects. The onset of fluid motion is considered above the curved geometrical contour described by $y = A(x+b)^{\frac{1-m}{2}}$, wherein the imposed stretching velocity near the surface conforms to the distribution $U_w = U_0(x+b)^m$. The surface is impermeable and free from melting resistance. A coupled homogeneous–heterogeneous reaction mechanism is considered, where a quartic autocatalytic reaction in the fluid phase (A) interacts with a first-order decay reaction on the catalyst-coated surface (B). The thermal field is influenced by nonlinear radiative heat transfer, and the surface temperature varies spatially as $T_w = A(x+b)^{\frac{1-m}{2}}$, while the far-field temperature remains uniform. The velocity components $u(x,y)$, $v(x,y)$, temperature $T(x,y)$, and concentration fields $a(x,y)$, $l(x,y)$ are analyzed within a boundary layer aligned along the x-axis, with y normal to the surface.

Employing the homogeneous–heterogeneous reaction paradigm initially promulgated by Chaudhary and Merkin [11] and later scrutinized with heightened analytical rigor by Lynch [19], an isothermal quartic autocatalytic reaction is envisaged within the confines of the boundary layer. This is especially pertinent to the circumstance wherein the concentration of catalyst B is markedly elevated at the interface. Furthermore, this concept has been extended and applied by Makinde and Animasaun [20, 21], as well as by Abegunrin et al. [1]

$$A + 3B \to 4B, \tag{3.1}$$

The chemical reaction is characterized by a rate of $k_1 al^3$, and exclusively a single isothermal first-order reaction of the specified type occurs on the upper horizontal surface of the paraboloid of rotation when a catalyst is introduced

$$A \to B, \tag{3.2}$$

The chemical reaction rate is represented by $k_s a$, whereas the concentrations of the reactants A and B are indicated by "a" and "l", respectively. The reaction rate coefficients, k_1 and k_s, cannot be strictly regarded as constants in this context because these parameters include all possible factors influencing the reaction rate, with the exception of concentration, which is explicitly taken into account in Eq. (3.1) and Eq. (3.2).

The governing boundary-layer equations take on the following form once Refs. [8, 17] are formulated:

$$\frac{\partial u}{\partial x} + \frac{\partial v}{\partial y} = 0, \tag{3.3}$$

$$u\frac{\partial u}{\partial x} + v\frac{\partial u}{\partial y} = \nu\left((1-n) + \sqrt{2}n\Gamma\left(\frac{\partial u}{\partial y}\right)\right)\frac{\partial^2 u}{\partial y^2} + \frac{\partial}{\partial x}\left(gxw\frac{m+1}{2}(T - T_\infty)\right) - \frac{\sigma B^2(x)}{\rho}u, \tag{3.4}$$

$$\begin{aligned} u\frac{\partial T}{\partial x} + v\frac{\partial T}{\partial y} &= \alpha\frac{\partial^2 T}{\partial y^2} - \frac{1}{\rho C_p}\frac{\partial q_r}{\partial y} + \tau\left(D_B\frac{\partial a}{\partial y}\frac{\partial T}{\partial y} + \frac{D_T}{T_\infty}\left(\frac{\partial T}{\partial y}\right)^2\right) \\ &\quad + \frac{Q_0[T_w - T_\infty]}{\rho C_p}Exp\left(-ny\sqrt{\frac{m+1}{2}}\sqrt{\frac{U_0}{\nu}}(x+b)^{\frac{m-1}{2}}\right). \end{aligned} \tag{3.5}$$

The conveyance of thermal energy through radiative modalities within the fluidic continuum is incorporated by employing the Rosseland diffusion approximation, which facilitates an analytical attenuation of the radiative transfer formalism under the postulation of an optically opacified regime

$$q_r = -\frac{4\sigma^*}{3k^*}\frac{\partial T^4}{\partial y} = -\frac{4\sigma^*}{3k^*}\frac{\partial}{\partial y}(T \times T \times T \times T). \tag{3.6}$$

In this case, σ^* and k^* represent the mean absorption coefficient and the Stefan–Boltzmann constant, respectively. Radiation is quickly scattered or absorbed in optically dense material. A diffusion term is added to the energy equation by Eq. (3.6), which reflects large temperature gradients that prevent T^4 from linearizing around T_∞.

Implicit differentiation and substitution yield the modified energy equation:

$$\begin{aligned} u\frac{\partial T}{\partial x} + v\frac{\partial T}{\partial y} &= \alpha\frac{\partial^2 T}{\partial y^2} + \frac{1}{\rho C_p}\frac{\partial}{\partial y}\left(\frac{4\sigma^*}{3k^*}\frac{\partial T^4}{\partial y}\right) + \tau\left(D_B\frac{\partial a}{\partial y}\frac{\partial T}{\partial y} + \frac{D_T}{T_\infty}\left(\frac{\partial T}{\partial y}\right)^2\right) \\ &\quad + \frac{Q_0[T_w - T_\infty]}{\rho C_p}Exp\left(-ny\sqrt{\frac{m+1}{2}}\sqrt{\frac{U_0}{\nu}}(x+b)^{\frac{m-1}{2}}\right). \end{aligned} \tag{3.7}$$

In accordance with the reaction scheme outlined in Eq. (3.1) and Eq. (3.2), the coupled homogeneous-heterogeneous reactive system dictating the concentration evolution of species A and B, is consequently established:

$$u\frac{\partial a}{\partial x} + v\frac{\partial a}{\partial y} = D_A\frac{\partial^2 a}{\partial y^2} - K_1 al^3, \tag{3.8}$$

$$u\frac{\partial l}{\partial x} + v\frac{\partial l}{\partial y} = D_B\frac{\partial^2 l}{\partial y^2} + K_1 al^3. \tag{3.9}$$

The homogeneous–heterogeneous catalytic interaction at the boundary is encapsulated through tailored boundary conditions governing the flow, acknowledging the chemical transformation of reactants A and B at the catalytic surface:

$$u = U_0(x+b)^m,\ v = 0,\ T = T_w(x),\ \frac{\partial a}{\partial y} = \frac{K_s a}{D_A},\ \frac{\partial l}{\partial y} = -\frac{K_s a}{D_B},\ \text{at}\ \ y = A(x+b)^{\frac{1-m}{2}}, \tag{3.10}$$

$$u \to 0, \qquad T \to T_\infty, \qquad a \to a_0, \qquad l \to 0, \qquad \text{as} \quad y \to \infty. \tag{3.11}$$

4. Non-dimensionalization and parametrization

Subsect to boundary conditions, Eqs. (3.3), (3.4), and (3.7) to Eq. (3.9) must be non-dimensionalized and parameterized. From Eqs. (3.10) and (3.11), Consider the following variables:

$$\eta = y\left(\frac{m+1}{2}\frac{U_o}{\vartheta}\right)^{1/2}(x+b)^{\frac{m-1}{2}},\ T_w = A(x+b)^{\frac{1-m}{2}},\ \theta = \frac{T-T_\infty}{T_w-T_\infty},\quad \frac{T}{T_\infty} = [1+\theta_w\theta-\theta],$$
$$\psi(x,y) = f\left(\frac{2}{m+1}\right)(\vartheta U_o)^{1/2}(x+b)^{\frac{m+1}{2}},\qquad g(\eta) = \frac{a}{a_o},\qquad h(\eta) = \frac{\ell}{a_o}.$$

Together with variables:

$$Gr = \frac{gw(T_w-T_\infty)}{U_o^2(x+b)^{2m-1}},\quad \theta_w = \frac{T_w}{T_\infty},\quad \Lambda = \frac{K_s}{D_A\left(\frac{m+1}{2}\frac{U_o}{\vartheta}\right)^{1/2}(x+b)^{\frac{m-1}{2}}},\quad Re_x = \frac{U_w(x+b)}{\vartheta},$$
$$\gamma = \frac{Q_o}{\rho C_p U_o(x+b)^{m-1}},\quad Pr = \frac{\rho C_p\vartheta}{k},\quad N_b = \frac{\tau D_B a_o \rho C_p}{k},\quad N_t = \frac{\tau D_T(T_w-T_\infty)\rho C_p}{T_\infty k},$$
$$Rd = \frac{4\sigma^* T_\infty^3}{kk^*},\quad Sc_a = \frac{\vartheta}{D_A},\quad Sc_b = \frac{\vartheta}{D_B},\quad K = \frac{K_1 a_o a_o^2}{U_o(x+b)^{m-1}},\quad \delta = \frac{D_B}{D_A},\ M = \frac{\sigma B_0^2}{\rho U_o}.$$

The dimensionless governing equation [8, 17] has the form of the continuity equation, which is naturally satisfied:

$$\left(1-n+nWe\frac{d^2f}{d\eta^2}\right)\frac{d^3f}{d\eta^3} - \left(\frac{2m}{m+1}\right)\frac{df}{d\eta}\frac{df}{d\eta} + f\frac{d^2f}{d\eta^2} + Gr\theta - \left(\frac{2}{m+1}\right)M\frac{df}{d\eta} = 0, \tag{4.1}$$

$$\left(1+\frac{4}{3}Rd[\theta(\theta_w-1)+1]^3\right)\frac{d^2\theta}{d\eta^2} + Prf\frac{d\theta}{d\eta} + (4Rd[\theta(\theta_w-1)+1]^2(\theta_w-1)+N_t)\frac{d\theta}{d\eta}\frac{d\theta}{d\eta}$$
$$+ N_b\frac{d\theta}{d\eta}\frac{dg}{d\eta} + \gamma Pr\left(\frac{2}{m+1}\right)Exp(-n\eta) = 0, \tag{4.2}$$

$$\frac{d^2g}{d\eta^2} + Sc_a f\frac{dg}{d\eta} - Sc_a K\frac{2}{m+1}gh^3 = 0, \tag{4.3}$$

$$\delta\frac{d^2h}{d\eta^2} + Sc_a f\frac{dh}{d\eta} + Sc_a K\frac{2}{m+1}gh^3 = 0. \tag{4.4}$$

Importantly, the lowest value of y does not correspond to the origin of the slot under the adopted non-dimensionalization scheme, thereby making $y = 0$ unsuitable for use in Eq. (3.10). As illustrated in Figure 1, imposing $y = 0$ along the upper paraboloid boundary is not valid.
Rather, when the flow initiates at $y = A(x+b)^{\frac{1-m}{2}}$, the minimum value of y aligns with the minimum of the similarity variable η as:

$$\eta = A\left(\frac{m+1}{2}\frac{U_o}{\vartheta}\right)^{1/2}, \tag{4.5}$$

The formula is $\chi = A\left(\frac{m+1}{2}\frac{U_a}{\vartheta}\right)^{1/2}$. This suggests that $\eta = \chi$ is the boundary condition appropriate to scale the boundary layer flow at the wall. The boundary condition turns into

$$\frac{df}{d\chi} = 1,\qquad f(\chi) = \chi\frac{1-m}{m+1},\qquad \theta(\chi) = 1,\quad \frac{dg}{d\chi} = \Lambda g(\chi),\qquad \delta\frac{dh}{d\chi} = -\Lambda g(\chi),\qquad \text{at } \chi = \eta, \tag{4.6}$$

$$\frac{df}{d\chi}\to 0,\quad \theta(\chi)\to 0,\quad g(\chi)\to 1,\quad h(\chi)\to 0\quad \text{as } \chi\to\infty. \tag{4.7}$$

The boundary conditions in Eqs. (4.6) and (4.7) are expressed in terms of χ, while the dimensionless equations in Eq. (4.1) to Eq. (4.4) are functions of η. To reframe the domain from $[\chi, \infty)$ to $[0, \infty)$, the transformations $F(\varsigma) = F(\eta - \chi) = f(\eta)$, $\Theta(\varsigma) = \Theta(\eta - \chi) = \theta(\eta)$, $G(\varsigma) = G(\eta - \chi) = g(\eta)$, and $H(\varsigma) = H(\eta - \chi) = h(\eta)$ are introduced.
This reformulation yields the definitive system of nonlinear ordinary differential equations:

$$\left(1 - n + nWe\frac{d^2F}{d\varsigma^2}\right)\frac{d^3F}{d\varsigma^3} - \left(\frac{2m}{m+1}\right)\frac{dF}{d\varsigma}\frac{dF}{d\varsigma} + F\frac{d^2F}{d\varsigma^2} + Gr\Theta - \left(\frac{2}{m+1}\right)M\frac{dF}{d\varsigma} = 0, \tag{4.8}$$

$$\begin{aligned}&\left(1 + \frac{4}{3}Rd[\Theta(\theta_w - 1) + 1]^3\right)\frac{d^2\Theta}{d\varsigma^2} + PrF\frac{d\Theta}{d\varsigma} + (4Rd[\Theta(\theta_w - 1) + 1]^2(\theta_w - 1) + N_t)\frac{d\Theta}{d\varsigma}\frac{d\Theta}{d\varsigma}\\ &+ N_b\frac{d\Theta}{d\varsigma}\frac{dG}{d\varsigma} + \gamma Pr\left(\frac{2}{m+1}\right)Exp(-n\varsigma) = 0,\end{aligned} \tag{4.9}$$

$$\frac{d^2G}{d\varsigma^2} + Sc_aF\frac{dG}{d\varsigma} - Sc_aK\frac{2}{m+1}GH^3 = 0, \tag{4.10}$$

$$\delta\frac{d^2H}{d\varsigma^2} + Sc_aF\frac{dH}{d\varsigma} + Sc_aK\frac{2}{m+1}GH^3 = 0. \tag{4.11}$$

Assuming that $\delta = 1$ because the diffusion coefficients D_A and D_B are modest, then

$$G(\varsigma) + H(\varsigma) = 1.$$

So, after the simplification:

$$\frac{d^2G}{d\varsigma^2} + Sc_aF\frac{dG}{d\varsigma} - Sc_aK\frac{2}{m+1}G(1 - G)^3 = 0. \tag{4.12}$$

Subsect to boundary conditions:

$$\frac{dF}{d\varsigma} = 1,\ F(\varsigma) = \chi\frac{1-m}{m+1},\ \Theta(\varsigma) = 1,\ \frac{dG}{d\varsigma} = \Lambda G(\varsigma) \text{ at } \quad \varsigma = 0, \tag{4.13}$$

$$\frac{dF}{d\varsigma} \to 0, \quad \Theta(\varsigma) \to 0, \quad G(\varsigma) \to 1 \quad \text{as} \quad \varsigma \to \infty. \tag{4.14}$$

As previously stated, the quantities of importance are the skin friction coefficient C_f and Nusselt number Nu:

$$C_f = \frac{\tau_w\mu}{\rho U_w^2\sqrt{\frac{m+1}{2}}}, \tag{4.15}$$

$$Nu = \frac{(x+b)q_w}{\kappa(T_w - T_\infty)\sqrt{\frac{m+1}{2}}}. \tag{4.16}$$

Here, q_w denotes the heat flux from the sheet, while τ_w represents the shear stress exerted on the stretching surface of the horizontal paraboloid of revolution:

$$\tau_w = (1-n)\frac{\partial u}{\partial y} + \frac{n\Gamma}{\sqrt{2}}\left(\frac{\partial u}{\partial y}\right)^2\Big|_{y=A(x+b)^{\frac{1-m}{2}}}, \tag{4.17}$$

$$q_w = -\left(\kappa + \frac{16\sigma^*T^3}{3k^*}\right)\left(\frac{\partial T}{\partial y}\right)\Big|_{y=A(x+b)^{\frac{1-m}{2}}}. \tag{4.18}$$

Upon substituting the similarity variables into Eq. (4.15) and Eq. (4.16), we obtain

$$C_{f_x} Re_x^{1/2} = (1-n)F''(0) + \frac{n}{\sqrt{2}} WeF''^2(0), \tag{4.19}$$

$$Nu_x Re_x^{-1/2} = -\left(1 + \frac{4}{3}Rd[1+(\theta_w - 1)\Theta]^3\right)\Theta'(0). \tag{4.20}$$

5. A Comprehensive examination of the Keller Box method's significance and applications

5.1. **Introduction: Addressing the Challenge of Nonlinear Systems.** In recent years, the scientific and engineering communities have witnessed a growing focus on resolving systems of nonlinear differential equations that describe complex physical phenomena. Professionals across numerous technological sectors routinely encounter nonlinear boundary-value problems that defy solution through traditional analytical means. While substantial advances have been achieved in creating innovative methods to address these nonlinear equations—particularly in domains such as fluid dynamics, biological modeling, financial forecasting, aeronautical design, and chemical process control—significant challenges persist.

This ongoing effort underscores the critical value of robust numerical techniques like the Keller Box Method. Originally formulated by Herbert B. Keller during the 1970s, this approach represents a sophisticated implicit finite-difference scheme specifically engineered to overcome these obstacles. It excels at solving parabolic partial differential equations and multi-point nonlinear boundary-value problems commonly arising in applied scientific research.

The technique operates through a logically structured two-phase procedure:

(1) **Equation Reduction and Spatial Discretization:** The process initiates by transforming higher-order partial differential or boundary-value equations into an extended system of first-order equations. The solution domain is then subdivided using a computational grid that uniquely positions unknown variables at the **midpoints** of grid cells, referred to as "boxes." This distinctive midpoint-centric framework constitutes the method's foundational characteristic.

(2) **Numerical Solution:** Subsequent integration of the first-order equations across each individual box employs the trapezoidal rule for approximation. This step yields a comprehensive set of implicit algebraic relations. The resulting nonlinear system undergoes linearization via **Newton's method** and is efficiently resolved using a **block-tridiagonal matrix algorithm**.

5.2. **Critical Value and Practical Utility: A Detailed Perspective.** The sustained relevance of the Keller Box Method arises from its exceptional blend of computational reliability, precision, and adaptability, establishing it as an indispensable instrument for addressing tangible scientific and industrial challenges.

5.2.1. *Computational Stability and Resilience.*

- **Inherent Implicit Structure:** Functioning as an implicit scheme, the method concurrently solves for unknown variables across numerous grid locations. This architecture ensures **unconditional stability** for a broad spectrum of problems, guaranteeing that numerical solutions remain convergent independent of selected time-step magnitude.
- **Practical Impact:** This stability property permits the use of considerably larger time increments compared to explicit techniques, which are constrained by strict step-size limits. This capability markedly enhances computational throughput for achieving steady-state conditions or simulating extended temporal periods, solidifying its status as a dependable choice for demanding technical applications.

5.2.2. *Effective Management of Nonlinear and Interconnected Systems.*

- **Iterative Linearization via Newton's Method:** The algorithm utilizes Newton's method to sequentially linearize the nonlinear algebraic equations derived from the discretization phase. This methodical approach is vital for managing mathematically stiff and intensely nonlinear systems.

- **Practical Impact:** This attribute renders the technique particularly powerful for deciphering intricate real-world scenarios that lack analytical solutions. It consistently handles coupled systems prevalent in sectors like magnetohydrodynamics (MHD), rheology of non-Newtonian fluids, transport in nanofluids, and deformation in viscoelastic materials, areas where alternative methods frequently falter.

5.2.3. *Enhanced Precision and Solution Convergence.*

- **Second-Order Numerical Accuracy:** The method achieves **second-order accuracy** ($O(\Delta x^2 + \Delta t^2)$) in both spatial and temporal dimensions. This indicates that the numerical error diminishes proportionally to the square of the refinement in grid spacing and time stepping.
- **Practical Impact:** It strikes an optimal equilibrium between computational expenditure and result fidelity, delivering high-quality solutions without necessitating impractical grid densities. Its rapid convergence behavior assures dependable outcomes through fewer computational cycles, establishing it as a superior tool for detailed numerical simulation.

5.2.4. *Wide-Ranging Applicability Across Disciplines.* The utility of the Keller Box Method extends beyond a narrow problem set, finding application in diverse scientific and engineering fields:

- **Fluid Mechanics and Boundary Layer Analysis:** It serves as a fundamental and reference-quality technique for resolving boundary layer equations (including Blasius flow, the Falkner-Skan equation, and flows through porous media). These applications are essential for aerodynamic profile design, internal flow assessment, and analyzing near-surface fluid behavior.
- **Thermal and Mass Transport Phenomena:** The method is widely adopted for simulating temperature distribution and concentration gradients in systems involving convective, diffusive, radiative, and reactive processes. This utility is crucial for developing effective thermal management systems, heat transfer equipment, and industrial reactors.
- **Contemporary Scientific Investigation:** It maintains its importance in progressive research areas such as microfluidic control, biological system modeling, economic analysis, and especially nanofluid thermophysics, as demonstrated by its persistent citation in modern academic literature.

5.2.5. *Methodical Framework and Instructional Benefit.*

- **Organized Computational Algorithm:** The technique offers a systematic, sequential protocol: reduce equation order, discretize the domain, linearize the resulting system, and obtain the solution. This structured progression minimizes potential numerical instabilities and renders the algorithm a versatile practical instrument adaptable to various problems without extensive customization.
- **Practical Impact:** For individuals seeking to apply the Keller-box method as a functional tool, its study imparts a thorough comprehension of essential numerical concepts including domain discretization, implicit iterative solution, Newton-based linearization, and structured matrix operations. This knowledge base provides a strong foundation for engaging with more advanced computational fluid dynamics principles.

5.2.6. *Reference Standard and Verification in Scientific Research.*

- **Established Benchmarking Role:** Within computational fluid dynamics and applied mathematics, solutions generated by the Keller Box Method are frequently adopted as **reference standards** for comparison.
- **Practical Impact:** Its proven dependability designates it as the preferred technique for confirming the validity of novel analytical approaches or alternative numerical schemes. Investigators rely on it to assess the precision of integrated software solvers, owing to its transparent and controllable calculation process.

6. Solution methodology

Following the mathematical formulation of the Keller–Box Method (KBM), a finite-difference based approach, this technique provides second-order accuracy while allowing flexibility in the choice of step size. Compared with conventional numerical methods, the KBM exhibits faster convergence and is particularly effective for boundary-layer flow problems, where other explicit techniques such as the Runge–Kutta method, BVP4c, or the shooting method may be less efficient. In this framework, higher-order partial differential equations are systematically reduced to a

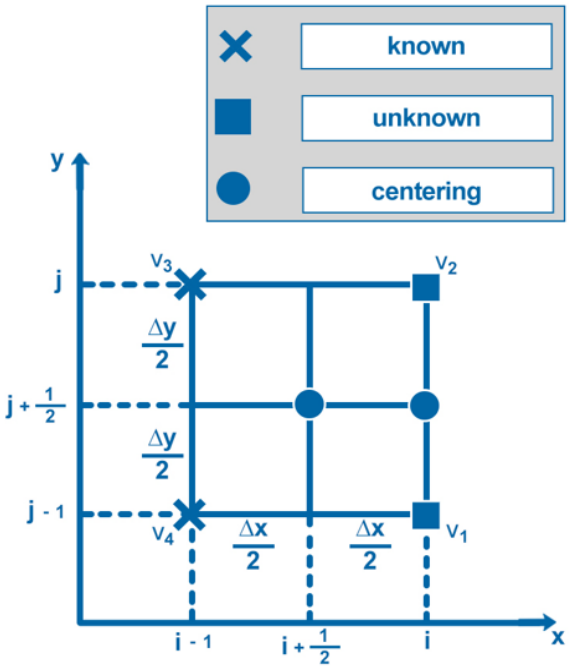

FIGURE 2. Two-dimensional Keller-Box method stencil.

system of first-order ordinary differential equations, which are then discretized using central difference formulas. The resulting matrix–vector system is solved efficiently through LU decomposition. The overall computational domain is truncated to a finite interval for practical implementation, and grid refinement is performed by reducing the step size until the desired accuracy is achieved. In essence, the Keller–Box scheme proceeds through four fundamental steps, offering several advantages over other numerical approaches for solving differential equations.

- It can handle complex boundary conditions such as mixed or nonlinear ones.
- It can achieve high accuracy and stability with relatively few boxes.
- It can be easily implemented on computers using a simple algorithm.

Steps involved in this method is explained in detail below:
(A). Reduction of the N^{th} order partial differential equation system to N 1^{st} order equations.
(B). Finite Difference Discretization.
(C). Quasi-linearization of Non-Linear Keller Algebraic Equations.
(D). Block-tridiagonal Elimination of Linear Keller Algebraic Equations.
Before discretizing Eqs. (4.8), (4.9), and (4.12), the finite difference method of Keller-Box is explained more details as follows. Figure 2 illustrates the Keller–Box method, in which higher-order derivatives are transformed into first-order derivatives. Although this transformation increases the computational cost per time step, the method remains highly efficient and well-suited for solving parabolic partial differential equations. As shown in Figure 2, the Keller–Box step size is taken as the average between j and $j-1$ along the y-axis, and between i and $i-1$ along the x-axis. The stencil is composed of four points, v_1, v_2, v_3, and v_4. Among these, v_3 and v_4 are prescribed by the boundary conditions, while v_1 and v_2 are computed using a half-step size in both directions, i.e., $\frac{\Delta x}{2}$ and $\frac{\Delta y}{2}$, which serve as centering steps. This approach provides second-order accuracy in both the x- and y-directions, and it can be applied with either uniform or non-uniform step sizes. For further clarity, the schematic in Figure 2 is also represented in Figure 3.

Figure 3 presents the Keller–Box method stencil in the case where the dependence is only on the spatial coordinate y, with a step size of $\frac{\Delta y}{2}$. The corresponding boundary conditions are specified at the lower boundary $y = 0$ and the upper boundary $y = N$. This one-dimensional stencil is essentially equivalent to the two-dimensional Keller–Box

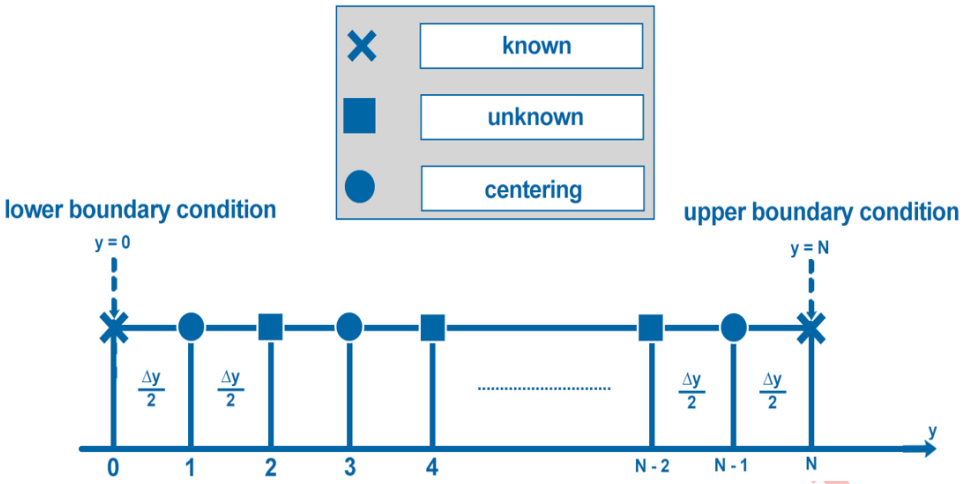

FIGURE 3. One-dimensional Keller-Box method stencil.

stencil shown in Figure 2, where the same half-step size $\frac{\Delta y}{2}$ is applied. For convenience in numerical implementation, Eqs. (4.8), (4.9), and (4.12) are reformulated into a system of first-order equations.

Steps involved in this method is explained in detail below:

Step A: The system of partial differential equations of N^{th} order was reduced to equations of N first order. Higher-order ODEs, such $F(x,\varsigma)$, are converted to first-order ODEs by adding the most recent set of variables mentioned below. $\Theta(x,\varsigma)$, $P(x,\varsigma)$, $Q(x,\varsigma)$, the values are $V(x,\varsigma)$, $E(x,\varsigma)$, and $H(x,\varsigma)$. Let's

$$F = F,\ F' = P,\ F'' = Q,\ F''' = Q',\ \Theta = \Theta,\ \Theta' = V,\ \Theta'' = V',\ G = G,\ G' = H,\ G'' = H'.$$

This process begins with writing the Eqs. (4.8), (4.9), and (4.12), as described below:

$$F''' = g(\varsigma, F, F', F'', \Theta), \tag{6.1}$$
$$\Theta'' = h(\varsigma, F, \Theta, \Theta', G'), \tag{6.2}$$
$$G'' = k(\varsigma, F, \Theta'', G, G'). \tag{6.3}$$

Transform the Eq. (6.1) to Eq. (6.3) into a system of first order ODEs in the second step:

$$F' = P, \tag{6.4}$$
$$P' = Q, \tag{6.5}$$
$$\Theta' = V, \tag{6.6}$$
$$G' = H. \tag{6.7}$$

Given this transformation, the following first order form is reduced by Eq. (6.1) to Eq. (6.3):

$$Q' = g(\varsigma, F, P, Q, \Theta), \tag{6.8}$$
$$V' = h(\varsigma, F, \Theta, V, H), \tag{6.9}$$
$$H' = k(\varsigma, F, V', G, H). \tag{6.10}$$

with the newly introduced variables, the boundary conditions become:

$$P(\varsigma) = 1,\ F(\varsigma) = \chi\frac{1-m}{m+1},\ \Theta(\varsigma) = 1,\ H(\varsigma) = \Lambda G(\varsigma) \text{ at } \varsigma = 0, \tag{6.11}$$
$$P(\varsigma) \to 0, \quad \Theta(\varsigma) \to 0, \quad G(\varsigma) \to 1 \quad \text{as} \quad \varsigma \to \infty. \tag{6.12}$$

Step B: The finite-difference method.
Additionally, the stencil represents domain discretization in the $x-\varsigma$ plane. With this mesh in mind, net points are

$$\begin{aligned} x^0 &= 0, \quad x^i = x^{i-1} + k_i, \quad i = 1,2,3,\ldots,I \\ \varsigma_0 &= 0, \quad \varsigma_s = \varsigma_{s-1} + h_s, \quad s = 1,2,3,\ldots,S \end{aligned} \tag{6.13}$$

where k_i and h_s represent the Δx and $\Delta\varsigma$ spacing, respectively.

$$\left(\frac{\partial(\ )}{\partial x}\right)^{i-\frac{1}{2}}_{s-1/2} = \frac{(\ )^i_{s-\frac{1}{2}} - (\ )^{i-1}_{s-\frac{1}{2}}}{k_i}, \tag{6.14}$$

$$\left(\frac{\partial(\ )}{\partial \varsigma}\right)^{i-\frac{1}{2}}_{s-1/2} = \frac{(\ )^i_{s-\frac{1}{2}} - (\ )^{i-1}_{s-\frac{1}{2}}}{h_s}, \tag{6.15}$$

$$(\ )^{i-\frac{1}{2}} = \frac{(\ )^{i-1}_s - (\ )^i_s}{2}, \quad (\ )^i_{s-\frac{1}{2}} = \frac{(\ )^i_{s-1} - (\ )^i_s}{2}. \tag{6.16}$$

The central difference technique is used to calculate the finite-difference form as follows:

$$F' = P \Rightarrow\ F' = (P)^i_{s-\frac{1}{2}} \Rightarrow\ \frac{(F^i_s - F^i_{s-1})}{h_s} = \frac{(P^i_s) + (P^i_{s-1})}{2}. \tag{6.17}$$

$$P' = Q \Rightarrow\ P' = (Q)^i_{s-\frac{1}{2}} \Rightarrow\ \frac{(P^i_s - P^i_{s-1})}{h_s} = \frac{(Q^i_s) + (Q^i_{s-1})}{2}. \tag{6.18}$$

$$\Theta' = V \Rightarrow\ \Theta' = (V)^i_{s-\frac{1}{2}} \Rightarrow\ \frac{(\Theta^i_s - \Theta^i_{s-1})}{h_s} = \frac{(V^i_s) + (V^i_{s-1})}{2}. \tag{6.19}$$

$$G' = H \Rightarrow\ G' = (H)^i_{s-\frac{1}{2}} \Rightarrow\ \frac{(G^i_s - G^i_{s-1})}{h_s} = \frac{(H^i_s) + (H^i_{s-1})}{2}. \tag{6.20}$$

Eq. (6.17) to Eq. (6.20) are centred at the $\left(x^{i-\frac{1}{2}}, \varsigma_{s-\frac{1}{2}}\right)$ locations, which are shown below:

$$F^i_s - F^i_{s-1} - \frac{h_s}{2}(P^i_s + P^i_{s-1}) = 0, \tag{6.21}$$

$$P^i_s - P^i_{s-1} - \frac{h_s}{2}(Q^i_s + Q^i_{s-1}) = 0, \tag{6.22}$$

$$\Theta^i_s - \Theta^i_{s-1} - \frac{h_s}{2}(V^i_s + V^i_{s-1}) = 0, \tag{6.23}$$

$$G^i_s - G^i_{s-1} - \frac{h_s}{2}(H^i_s + H^i_{s-1}) = 0, \tag{6.24}$$

$$\begin{aligned} &\left(1 - n + nWe\frac{h_s}{2}(Q^i_s + Q^i_{s-1})\right)(Q^i_s - Q^i_{s-1}) - \left(\frac{2m}{m+1}\right)\frac{h_s}{4}(P^i_s + P^i_{s-1})(P^i_s + P^i_{s-1}) \\ &\quad + \frac{h_s}{4}(F^i_s + F^i_{s-1})(Q^i_s + Q^i_{s-1}) + Gr\frac{h_s}{2}(\Theta^i_s + \Theta^i_{s-1}) - \left(\frac{2}{m+1}\right)M\frac{h_s}{2}(P^i_s + P^i_{s-1}) = 0, \end{aligned} \tag{6.25}$$

$$\begin{aligned} &\left(1 + \frac{4}{3}Rd[\Theta(\theta_w - 1) + 1]^3\right)(V^i_s - V^i_{s-1}) + Pr\frac{h_s}{4}(F^i_s + F^i_{s-1})(V^i_s + V^i_{s-1}) \\ &\quad + (4Rd[\frac{h_s}{2}(\Theta^i_s + \Theta^i_{s-1})(\theta_w - 1) + 1]^2(\theta_w - 1) + N_t)\frac{h_s}{4}(V^i_s + V^i_{s-1})(V^i_s + V^i_{s-1}) \\ &\quad + N_b\frac{h_s}{4}(V^i_s + V^i_{s-1})(H^i_s + H^i_{s-1}) + \gamma Pr\left(\frac{2}{m+1}\right)Exp(-n\varsigma) = 0, \end{aligned} \tag{6.26}$$

$$(H^i_s - H^i_{s-1}) + Sc_a\frac{h_s}{4}(F^i_s + F^i_{s-1})(H^i_s + H^i_{s-1}) - Sc_aK\frac{2}{m+1}\frac{h_s}{2}(G^i_s + G^i_{s-1})(1 - \frac{h_s}{2}(G^i_s + G^i_{s-1}))^3 = 0. \tag{6.27}$$

Subsect to boundary conditions:

$$P(x,\varsigma)=1,\quad F(x,\varsigma)=\chi\frac{1-m}{m+1},\quad \Theta(x,\varsigma)=1,\quad H(x,\varsigma)=\Lambda G(x,\varsigma),\quad \text{at}\quad \varsigma=0, \tag{6.28}$$

$$P(x,\varsigma)\to 0,\qquad \Theta(x,\varsigma)\to 0,\qquad G(x,\varsigma)\to 1\qquad \text{as}\quad \varsigma\to\infty. \tag{6.29}$$

For $s=2,3,\ldots,S$, Eq. (6.8) to Eq. (6.10) are applied, and the transformed boundary layer thickness, ς_s, is sufficiently large to be outside the boundary layer's edge (Keller and Cebeci [15]). At $x=x^n$, the boundary conditions yield are

$$P_1^n=1,\qquad F_1^n=\chi\frac{1-m}{m+1},\qquad \Theta_1^n=1,\qquad H_1^n=\Lambda G_1^n. \tag{6.30}$$

$$P_S^n\to 0,\quad \Theta_S^n\to 0,\quad G_S^n\to 1. \tag{6.31}$$

Step C: Newton's linearization approach.
Eq. (6.8) to Eq. (6.10) are linearized using Newton's technique.

$$\begin{aligned}
F_s^{(i+1)}&=F_s^{(i)}+\delta F_s^{(i)},\\
P_s^{(i+1)}&=P_s^{(i)}+\delta P_s^{(i)},\\
Q_s^{(i+1)}&=Q_s^{(i)}+\delta Q_s^{(i)},\\
\Theta_s^{(i+1)}&=\Theta_s^{(i)}+\delta\Theta_s^{(i)},\\
V_s^{(i+1)}&=V_s^{(i)}+\delta V_s^{(i)},\\
G_s^{(i+1)}&=G_s^{(i)}+\delta G_s^{(i)},\\
H_s^{(i+1)}&=H_s^{(i)}+\delta H_s^{(i)}.
\end{aligned} \tag{6.32}$$

By invoking above expressions in Eq. (6.8) to Eq. (6.10) and neglecting quadratic and higher order terms in $\delta F_s^{(i)}$, $\delta P_s^{(i)}$, $\delta Q_s^{(i)}$, $\delta\Theta_s^{(i)}$, $\delta V_s^{(i)}$, $\delta G_s^{(i)}$, $\delta H_s^{(i)}$, we reached at following tri-diagonal system

$$\delta F_s-\delta F_{s-1}-\frac{h_s}{2}(\delta P_s+\delta P_{s-1})=(r_1)_{s-\frac{1}{2}}, \tag{6.33}$$

$$\delta P_s-\delta P_{s-1}-\frac{h_s}{2}(\delta Q_s+\delta Q_{s-1})=(r_2)_{s-\frac{1}{2}}, \tag{6.34}$$

$$\delta\Theta_s-\delta\Theta_{s-1}-\frac{h_s}{2}(\delta V_s+\delta V_{s-1})=(r_3)_{s-\frac{1}{2}}, \tag{6.35}$$

$$\delta G_s-\delta G_{s-1}-\frac{h_s}{2}(\delta H_s+\delta H_{s-1})=(r_4)_{s-\frac{1}{2}}, \tag{6.36}$$

$$\begin{aligned}
&(a_1)_s\delta F_s+(a_2)_s\delta F_{s-1}+(a_3)_s\delta P_s+(a_4)_s\delta P_{s-1}+(a_5)_s\delta Q_s+(a_6)_s\delta Q_{s-1}+(a_7)_s\delta\Theta_s+(a_8)_s\delta\Theta_{s-1}\\
&+(a_9)_s\delta V_s+(a_{10})_s\delta V_{s-1}+(a_{11})_s\delta G_s+(a_{12})_s\delta G_{s-1}+(a_{13})_s\delta H_s+(a_{14})_s\delta H_{s-1}=(r_5)_{s-\frac{1}{2}},
\end{aligned} \tag{6.37}$$

$$\begin{aligned}
&(b_1)_s\delta F_s+(b_2)_s\delta F_{s-1}+(b_3)_s\delta P_s+(b_4)_s\delta P_{s-1}+(b_5)_s\delta Q_s+(b_6)_s\delta Q_{s-1}+(b_7)_s\delta\Theta_s+(b_8)_s\delta\Theta_{s-1}\\
&+(b_9)_s\delta V_s+(b_{10})_s\delta V_{s-1}+(b_{11})_s\delta G_s+(b_{12})_s\delta G_{s-1}+(b_{13})_s\delta H_s+(b_{14})_s\delta H_{s-1}=(r_6)_{s-\frac{1}{2}},
\end{aligned} \tag{6.38}$$

$$\begin{aligned}
&(c_1)_s\delta F_s+(c_2)_s\delta F_{s-1}+(c_3)_s\delta P_s+(c_4)_s\delta P_{s-1}+(c_5)_s\delta Q_s+(c_6)_s\delta Q_{s-1}+(c_7)_s\delta\Theta_s+(c_8)_s\delta\Theta_{s-1}\\
&+(c_9)_s\delta V_s+(c_{10})_s\delta V_{s-1}+(c_{11})_s\delta G_s+(c_{12})_s\delta G_{s-1}+(c_{13})_s\delta H_s+(c_{14})_s\delta H_{s-1}=(r_7)_{s-\frac{1}{2}}.
\end{aligned} \tag{6.39}$$

Boundary condition becomes:

$$\begin{aligned}&(\delta F)_1 = 0, \quad (\delta P)_1 = 0, \quad (\delta Q)_1 = 0, \quad (\delta \Theta)_1 = 0, \quad (\delta V)_1 = 0,\\ &(\delta G)_1 = 0, \quad (\delta H)_1 = 0 \quad \dots \ (\delta P)_{s-1}, \quad (\delta \Theta)_{s-1}, \quad (\delta G)_{s-1}.\end{aligned} \tag{6.40}$$

Step D: Tridiagonal system of solution.
Cebeci and Bradshaw [10] found that the linearized difference equations (6.33) to (6.39) can be solved using the block-elimination approach due to the system's block-tridiagonal structure. The block-tridiagonal structure in this case is unique because it is made up of block matrices, or equations, rather than variables or constants.The matrix-vector representation of Eq. (6.33) to Eq. (6.39) is as follows
For $s = 1$;

$$\delta F_1 - \delta F_0 - \frac{h_1}{2}(\delta P_1 + \delta P_0) = (r_1)_{1-\frac{1}{2}}, \tag{6.41}$$

$$\delta P_1 - \delta P_0 - \frac{h_1}{2}(\delta Q_1 + \delta Q_0) = (r_2)_{1-\frac{1}{2}}, \tag{6.42}$$

$$\delta \Theta_1 - \delta \Theta_0 - \frac{h_1}{2}(\delta V_1 + \delta V_0) = (r_3)_{1-\frac{1}{2}}, \tag{6.43}$$

$$\delta G_1 - \delta G_0 - \frac{h_1}{2}(\delta H_1 + \delta H_0) = (r_4)_{1-\frac{1}{2}}, \tag{6.44}$$

$$\begin{aligned}&(a_1)_1\delta F_1 + (a_2)_1\delta F_0 + (a_3)_1\delta P_1 + (a_4)_1\delta P_0 + (a_5)_1\delta Q_1 + (a_6)_1\delta Q_0 + (a_7)_1\delta \Theta_1 + (a_8)_1\delta \Theta_0 +\\ &(a_9)_1\delta V_1 + (a_{10})_1\delta V_0 + (a_{11})_1\delta G_1 + (a_{12})_1\delta G_0 + (a_{13})_1\delta H_1 + (a_{14})_1\delta H_0 = (r_5)_{1-\frac{1}{2}},\end{aligned} \tag{6.45}$$

$$\begin{aligned}&(b_1)_1\delta F_1 + (b_2)_1\delta F_0 + (b_3)_1\delta P_1 + (b_4)_1\delta P_0 + (b_5)_1\delta Q_1 + (b_6)_1\delta Q_0 + (b_7)_1\delta \Theta_1 + (b_8)_1\delta \Theta_0 +\\ &(b_9)_1\delta V_1 + (b_{10})_1\delta V_0 + (b_{11})_1\delta G_1 + (b_{12})_1\delta G_0 + (b_{13})_1\delta H_1 + (b_{14})_1\delta H_0 = (r_6)_{1-\frac{1}{2}},\end{aligned} \tag{6.46}$$

$$\begin{aligned}&(c_1)_1\delta F_1 + (c_2)_1\delta F_0 + (c_3)_1\delta P_1 + (c_4)_1\delta P_0 + (c_5)_1\delta Q_1 + (c_6)_1\delta Q_0 + (c_7)_1\delta \Theta_1 + (c_8)_1\delta \Theta_0 +\\ &(c_9)_1\delta V_1 + (c_{10})_1\delta V_0 + (c_{11})_1\delta G_1 + (c_{12})_1\delta G_0 + (c_{13})_1\delta H_1 + (c_{14})_1\delta H_0 = (r_7)_{1-\frac{1}{2}},\end{aligned} \tag{6.47}$$

In matrix formula,

$$\begin{bmatrix} 0 & 0 & 0 & 1 & 0 & 0 & 0 \\ -h/2 & 0 & 0 & 0 & -h/2 & 0 & 0 \\ 0 & -h/2 & 0 & 0 & 0 & -h/2 & 0 \\ 0 & 0 & -1 & 0 & 0 & 0 & -h/2 \\ (a_6)_1 & (a_{10})_1 & (a_{12})_1 & (a_1)_1 & (a_5)_1 & (a_9)_1 & (a_{13})_1 \\ (b_6)_1 & (b_{10})_1 & (b_{12})_1 & (b_1)_1 & (b_5)_1 & (b_9)_1 & (b_{13})_1 \\ (c_6)_1 & (c_{10})_1 & (c_{12})_1 & (c_1)_1 & (c_5)_1 & (c_9)_1 & (c_{13})_1 \end{bmatrix} \begin{bmatrix} (\delta Q)_1 \\ (\delta V)_1 \\ (\delta G)_1 \\ (\delta F)_2 \\ (\delta Q)_2 \\ (\delta V)_2 \\ (\delta H)_2 \end{bmatrix}$$
$$+ \begin{bmatrix} -h/2 & 0 & 0 & 0 & 0 & 0 & 0 \\ 1 & 0 & 0 & 0 & 0 & 0 & 0 \\ 0 & 1 & 0 & 0 & 0 & 0 & 0 \\ 0 & 0 & 1 & 0 & 0 & 0 & 0 \\ (a_3)_1 & (a_7)_1 & (a_{11})_1 & 0 & 0 & 0 & 0 \\ (b_3)_1 & (b_7)_1 & (b_{11})_1 & 0 & 0 & 0 & 0 \\ (c_3)_1 & (c_7)_1 & (c_{11})_1 & 0 & 0 & 0 & 0 \end{bmatrix} \begin{bmatrix} (\delta P)_2 \\ (\delta \Theta)_2 \\ (\delta G)_2 \\ (\delta F)_3 \\ (\delta Q)_3 \\ (\delta V)_3 \\ (\delta H)_3 \end{bmatrix} = \begin{bmatrix} (r_1)_{1-\frac{1}{2}} \\ (r_2)_{1-\frac{1}{2}} \\ (r_3)_{1-\frac{1}{2}} \\ (r_4)_{1-\frac{1}{2}} \\ (r_5)_{1-\frac{1}{2}} \\ (r_6)_{1-\frac{1}{2}} \\ (r_7)_{1-\frac{1}{2}} \end{bmatrix}. \tag{6.48}$$

For $s = 2$;

$$\delta F_2 - \delta F_1 - \frac{h_2}{2}(\delta P_2 + \delta P_1) = (r_1)_{2-\frac{1}{2}}, \tag{6.49}$$

$$\delta P_2 - \delta P_1 - \frac{h_2}{2}(\delta Q_2 + \delta Q_1) = (r_2)_{2-\frac{1}{2}}, \tag{6.50}$$

$$\delta \Theta_2 - \delta \Theta_1 - \frac{h_2}{2}(\delta V_2 + \delta V_1) = (r_3)_{2-\frac{1}{2}}, \tag{6.51}$$

$$\delta G_2 - \delta G_1 - \frac{h_2}{2}(\delta H_2 + \delta H_1) = (r_4)_{2-\frac{1}{2}}, \tag{6.52}$$

$$\begin{aligned}&(a_1)_2\delta F_2 + (a_2)_2\delta F_1 + (a_3)_2\delta P_2 + (a_4)_2\delta P_1 + (a_5)_2\delta Q_2 + (a_6)_2\delta Q_1 + (a_7)_2\delta \Theta_2 + (a_8)_2\delta \Theta_1 + \\ &(a_9)_2\delta V_2 + (a_{10})_2\delta V_1 + (a_{11})_2\delta G_2 + (a_{12})_2\delta G_1 + (a_{13})_2\delta H_2 + (a_{14})_2\delta H_1 = (r_5)_{2-\frac{1}{2}},\end{aligned} \tag{6.53}$$

$$\begin{aligned}&(b_1)_2\delta F_2 + (b_2)_2\delta F_1 + (b_3)_2\delta P_2 + (b_4)_2\delta P_1 + (b_5)_2\delta Q_2 + (b_6)_2\delta Q_1 + (b_7)_2\delta \Theta_2 + (b_8)_2\delta \Theta_1 + \\ &(b_9)_2\delta V_2 + (b_{10})_2\delta V_1 + (b_{11})_2\delta G_2 + (b_{12})_2\delta G_1 + (b_{13})_2\delta H_2 + (b_{14})_2\delta H_1 = (r_6)_{2-\frac{1}{2}},\end{aligned} \tag{6.54}$$

$$\begin{aligned}&(c_1)_2\delta F_2 + (c_2)_2\delta F_1 + (c_3)_2\delta P_2 + (c_4)_2\delta P_1 + (c_5)_2\delta Q_2 + (c_6)_2\delta Q_1 + (c_7)_2\delta \Theta_2 + (c_8)_2\delta \Theta_1 + \\ &(c_9)_2\delta V_2 + (c_{10})_2\delta V_1 + (c_{11})_2\delta G_2 + (c_{12})_2\delta G_1 + (c_{13})_2\delta H_2 + (c_{14})_2\delta H_1 = (r_7)_{2-\frac{1}{2}},\end{aligned} \tag{6.55}$$

In matrix formula,

$$\begin{aligned}&\begin{bmatrix} 0 & 0 & 0 & -1 & 0 & 0 & 0 \\ 0 & 0 & 0 & 0 & -h/2 & 0 & 0 \\ 0 & 0 & 0 & 0 & 0 & -h/2 & 0 \\ 0 & 0 & 0 & 0 & 0 & 0 & -h/2 \\ 0 & 0 & 0 & (a_2)_2 & (a_6)_2 & (a_{10})_2 & (a_{14})_2 \\ 0 & 0 & 0 & (b_2)_2 & (b_6)_2 & (b_{10})_2 & (b_{14})_2 \\ 0 & 0 & 0 & (c_2)_2 & (c_6)_2 & (c_{10})_2 & (c_{14})_2 \end{bmatrix} \begin{bmatrix} (\delta Q)_1 \\ (\delta V)_1 \\ (\delta G)_1 \\ (\delta F)_2 \\ (\delta Q)_2 \\ (\delta V)_2 \\ (\delta H)_2 \end{bmatrix} \\ &+ \begin{bmatrix} -h/2 & 0 & 0 & 1 & 0 & 0 & 0 \\ -1 & 0 & 0 & 0 & -h/2 & 0 & 0 \\ 0 & -1 & 0 & 0 & 0 & -h/2 & 0 \\ 0 & 0 & -1 & 0 & 0 & 0 & -h/2 \\ (a_4)_2 & (a_8)_2 & (a_{12})_2 & (a_1)_2 & (a_5)_2 & (a_9)_2 & (a_{13})_2 \\ (b_4)_2 & (b_8)_2 & (b_{12})_2 & (b_1)_2 & (b_5)_2 & (b_9)_2 & (b_{13})_2 \\ (c_4)_2 & (c_8)_2 & (c_{12})_2 & (c_1)_2 & (c_5)_2 & (c_9)_2 & (c_{13})_2 \end{bmatrix} \begin{bmatrix} (\delta P)_2 \\ (\delta \Theta)_2 \\ (\delta G)_2 \\ (\delta F)_3 \\ (\delta Q)_3 \\ (\delta V)_3 \\ (\delta H)_3 \end{bmatrix} \\ &+ \begin{bmatrix} -h/2 & 0 & 0 & 0 & 0 & 0 & 0 \\ 1 & 0 & 0 & 0 & 0 & 0 & 0 \\ 0 & 1 & 0 & 0 & 0 & 0 & 0 \\ 0 & 0 & 1 & 0 & 0 & 0 & 0 \\ (a_3)_2 & (a_7)_2 & (a_{11})_2 & 0 & 0 & 0 & 0 \\ (b_3)_2 & (b_7)_2 & (b_{11})_2 & 0 & 0 & 0 & 0 \\ (c_3)_2 & (c_7)_2 & (c_{11})_2 & 0 & 0 & 0 & 0 \end{bmatrix} \begin{bmatrix} (\delta P)_3 \\ (\delta \Theta)_3 \\ (\delta G)_3 \\ (\delta F)_4 \\ (\delta Q)_4 \\ (\delta V)_4 \\ (\delta H)_4 \end{bmatrix} = \begin{bmatrix} (r_1)_{2-\frac{1}{2}} \\ (r_2)_{2-\frac{1}{2}} \\ (r_3)_{2-\frac{1}{2}} \\ (r_4)_{2-\frac{1}{2}} \\ (r_5)_{2-\frac{1}{2}} \\ (r_6)_{2-\frac{1}{2}} \\ (r_7)_{2-\frac{1}{2}} \end{bmatrix}. \end{aligned} \tag{6.56}$$

For $s = S-1$;

$$\delta F_{S-1} - \delta F_{(S-1)-1} - \frac{h_{S-1}}{2}(\delta P_{S-1} + \delta P_{(S-1)-1}) = (r_1)_{(S-1)-\frac{1}{2}}, \tag{6.57}$$

$$\delta P_{S-1} - \delta P_{(S-1)-1} - \frac{h_{S-1}}{2}(\delta Q_{S-1} + \delta Q_{(S-1)-1}) = (r_2)_{(S-1)-\frac{1}{2}}, \tag{6.58}$$

$$\delta \Theta_{S-1} - \delta \Theta_{(S-1)-1} - \frac{h_{S-1}}{2}(\delta V_{S-1} + \delta V_{(S-1)-1}) = (r_3)_{(S-1)-\frac{1}{2}}, \tag{6.59}$$

$$\delta G_{S-1} - \delta G_{(S-1)-1} - \frac{h_{S-1}}{2}(\delta H_{S-1} + \delta H_{S-1-1}) = (r_4)_{(S-1)-\frac{1}{2}}, \tag{6.60}$$

$$\begin{aligned}&(a_1)_{S-1}\delta F_{S-1} + (a_2)_{S-1}\delta F_{(S-1)-1} + (a_3)_{S-1}\delta P_{S-1} + (a_4)_{S-1}\delta P_{(S-1)-1} + (a_5)_{S-1}\delta Q_{S-1} + (a_6)_{S-1}\\ &\delta Q_{(S-1)-1} + (a_7)_{S-1}\delta \Theta_{S-1} + (a_8)_{S-1}\delta \Theta_{(S-1)-1} + (a_9)_{S-1}\delta V_{S-1} + (a_{10})_{S-1}\delta V_{(S-1)-1}\\ &+ (a_{11})_{S-1}\delta G_{S-1} + (a_{12})_{S-1}\delta G_{(S-1)-1} + (a_{13})_{S-1}\delta H_{S-1} + (a_{14})_{S-1}\delta H_{(S-1)-1} = (r_5)_{(S-1)-\frac{1}{2}},\end{aligned} \tag{6.61}$$

$$\begin{aligned}&(b_1)_{S-1}\delta F_{S-1} + (b_2)_{S-1}\delta F_{(S-1)-1} + (b_3)_{S-1}\delta P_{S-1} + (b_4)_{S-1}\delta P_{(S-1)-1} + (b_5)_{S-1}\delta Q_{S-1} + (b_6)_{S-1}\\ &\delta Q_{(S-1)-1} + (b_7)_{S-1}\delta \Theta_{S-1} + (b_8)_{S-1}\delta \Theta_{(S-1)-1} + (b_9)_{S-1}\delta V_{S-1} + (b_{10})_{S-1}\delta V_{(S-1)-1}\\ &+ (b_{11})_{S-1}\delta G_{S-1} + (b_{12})_{S-1}\delta G_{(S-1)-1} + (b_{13})_{S-1}\delta H_{S-1} + (b_{14})_{S-1}\delta H_{(S-1)-1} = (r_6)_{(S-1)-\frac{1}{2}},\end{aligned} \tag{6.62}$$

$$\begin{aligned}&(c_1)_{S-1}\delta F_{S-1} + (c_2)_{S-1}\delta F_{(S-1)-1} + (c_3)_{S-1}\delta P_{S-1} + (c_4)_{S-1}\delta P_{(S-1)-1} + (c_5)_{S-1}\delta Q_{S-1} + (c_6)_{S-1}\\ &\delta Q_{(S-1)-1} + (c_7)_{S-1}\delta \Theta_{S-1} + (c_8)_{S-1}\delta \Theta_{(S-1)-1} + (c_9)_{S-1}\delta V_{S-1} + (c_{10})_{S-1}\delta V_{(S-1)-1}\\ &+ (c_{11})_{S-1}\delta G_{S-1} + (c_{12})_{S-1}\delta G_{(S-1)-1} + (c_{13})_{S-1}\delta H_{S-1} + (c_{14})_{S-1}\delta H_{(S-1)-1} = (r_7)_{(S-1)-\frac{1}{2}}.\end{aligned} \tag{6.63}$$

In matrix formula,

$$\begin{bmatrix} 0 & 0 & 0 & -1 & 0 & 0 & 0 \\ 0 & 0 & 0 & 0 & -h/2 & 0 & 0 \\ 0 & 0 & 0 & 0 & 0 & -h/2 & 0 \\ 0 & 0 & 0 & 0 & 0 & 0 & -h/2 \\ 0 & 0 & 0 & (a_2)_{S-1} & (a_6)_{S-1} & (a_{10})_{S-1} & (a_{14})_{S-1} \\ 0 & 0 & 0 & (b_2)_{S-1} & (b_6)_{S-1} & (b_{10})_{S-1} & (b_{14})_{S-1} \\ 0 & 0 & 0 & (c_2)_{S-1} & (c_6)_{S-1} & (c_{10})_{S-1} & (c_{14})_{S-1} \end{bmatrix} \begin{bmatrix} (\delta Q)_1 \\ (\delta V)_1 \\ (\delta G)_1 \\ (\delta F)_2 \\ (\delta Q)_2 \\ (\delta V)_2 \\ (\delta H)_2 \end{bmatrix}$$

$$+ \begin{bmatrix} -h/2 & 0 & 0 & 1 & 0 & 0 & 0 \\ -1 & 0 & 0 & 0 & -h/2 & 0 & 0 \\ 0 & -1 & 0 & 0 & 0 & -h/2 & 0 \\ 0 & 0 & -1 & 0 & 0 & 0 & -h/2 \\ (a_4)_{S-1} & (a_8)_{S-1} & (a_{12})_{S-1} & (a_1)_{S-1} & (a_5)_{S-1} & (a_9)_{S-1} & (a_{13})_{S-1} \\ (b_4)_{S-1} & (b_8)_{S-1} & (b_{12})_{S-1} & (b_1)_{S-1} & (b_5)_{S-1} & (b_9)_{S-1} & (b_{13})_{S-1} \\ (c_4)_{S-1} & (c_8)_{S-1} & (c_{12})_{S-1} & (c_1)_{S-1} & (c_5)_{S-1} & (c_9)_{S-1} & (c_{13})_{S-1} \end{bmatrix} \begin{bmatrix} (\delta P)_2 \\ (\delta \Theta)_2 \\ (\delta G)_2 \\ (\delta F)_3 \\ (\delta Q)_3 \\ (\delta V)_3 \\ (\delta H)_3 \end{bmatrix}$$

$$+ \begin{bmatrix} -h/2 & 0 & 0 & 0 & 0 & 0 & 0 \\ 1 & 0 & 0 & 0 & 0 & 0 & 0 \\ 0 & 1 & 0 & 0 & 0 & 0 & 0 \\ 0 & 0 & 1 & 0 & 0 & 0 & 0 \\ (a_3)_{S-1} & (a_7)_{S-1} & (a_{11})_{S-1} & 0 & 0 & 0 & 0 \\ (b_3)_{S-1} & (b_7)_{S-1} & (b_{11})_{S-1} & 0 & 0 & 0 & 0 \\ (c_3)_{S-1} & (c_7)_{S-1} & (c_{11})_{S-1} & 0 & 0 & 0 & 0 \end{bmatrix} \begin{bmatrix} (\delta P)_3 \\ (\delta \Theta)_3 \\ (\delta G)_3 \\ (\delta F)_4 \\ (\delta Q)_4 \\ (\delta V)_4 \\ (\delta H)_4 \end{bmatrix} = \begin{bmatrix} (r_1)_{(S-1)-\frac{1}{2}} \\ (r_2)_{(S-1)-\frac{1}{2}} \\ (r_3)_{(S-1)-\frac{1}{2}} \\ (r_4)_{(S-1)-\frac{1}{2}} \\ (r_5)_{(S-1)-\frac{1}{2}} \\ (r_6)_{(S-1)-\frac{1}{2}} \\ (r_7)_{(S-1)-\frac{1}{2}} \end{bmatrix}. \tag{6.64}$$

For $s = S$:

$$\delta F_S - \delta F_{S-1} - \frac{h_S}{2}(\delta P_S + \delta P_{S-1}) = (r_1)_{S-\frac{1}{2}}, \tag{6.65}$$

$$\delta P_S - \delta P_{S-1} - \frac{h_S}{2}(\delta Q_S + \delta Q_{S-1}) = (r_2)_{S-\frac{1}{2}}, \tag{6.66}$$

$$\delta \Theta_S - \delta \Theta_{S-1} - \frac{h_S}{2}(\delta V_S + \delta V_{S-1}) = (r_3)_{S-\frac{1}{2}}, \tag{6.67}$$

$$\delta G_S - \delta G_{S-1} - \frac{h_S}{2}(\delta H_S + \delta H_{S-1}) = (r_4)_{S-\frac{1}{2}}, \tag{6.68}$$

$$\begin{aligned}(a_1)_S\delta F_S + (a_2)_S\delta F_{S-1} + (a_3)_S\delta P_S + (a_4)_S\delta P_{S-1} + (a_5)_S\delta Q_S + (a_6)_S\delta Q_{S-1} + (a_7)_S\delta \Theta_S + (a_8)_S\delta \Theta_{S-1}\\ + (a_9)_S\delta V_S + (a_{10})_S\delta V_{S-1} + (a_{11})_S\delta G_S + (a_{12})_S\delta G_{S-1} + (a_{13})_S\delta H_S + (a_{14})_S\delta H_{S-1} = (r_5)_{S-\frac{1}{2}},\end{aligned} \tag{6.69}$$

$$\begin{aligned}(b_1)_S\delta F_S + (b_2)_S\delta F_{S-1} + (b_3)_S\delta P_S + (b_4)_S\delta P_{S-1} + (b_5)_S\delta Q_S + (b_6)_S\delta Q_{S-1} + (b_7)_S\delta \Theta_S + (b_8)_S\delta \Theta_{S-1}\\ + (b_9)_S\delta V_S + (b_{10})_S\delta V_{S-1} + (b_{11})_S\delta G_S + (b_{12})_S\delta G_{S-1} + (b_{13})_S\delta H_S + (b_{14})_S\delta H_{S-1} = (r_6)_{S-\frac{1}{2}},\end{aligned} \tag{6.70}$$

$$\begin{aligned}(c_1)_S\delta F_S + (c_2)_S\delta F_{S-1} + (c_3)_S\delta P_S + (c_4)_S\delta P_{S-1} + (c_5)_S\delta Q_S + (c_6)_S\delta Q_{S-1} + (c_7)_S\delta \Theta_S + (c_8)_S\delta \Theta_{S-1}\\ + (c_9)_S\delta V_S + (c_{10})_S\delta V_{S-1} + (c_{11})_S\delta G_S + (c_{12})_S\delta G_{S-1} + (c_{13})_S\delta H_S + (c_{14})_S\delta H_{S-1} = (r_7)_{S-\frac{1}{2}}.\end{aligned} \tag{6.71}$$

In matrix formula,

$$\begin{bmatrix} 0 & 0 & 0 & -1 & 0 & 0 & 0 \\ 0 & 0 & 0 & 0 & -h/2 & 0 & 0 \\ 0 & 0 & 0 & 0 & 0 & -h/2 & 0 \\ 0 & 0 & 0 & 0 & 0 & 0 & -h/2 \\ 0 & 0 & 0 & (a_2)_S & (a_6)_S & (a_{10})_S & (a_{14})_S \\ 0 & 0 & 0 & (b_2)_S & (b_6)_S & (b_{10})_S & (b_{14})_S \\ 0 & 0 & 0 & (c_2)_S & (c_6)_S & (c_{10})_S & (c_{14})_S \end{bmatrix} \begin{bmatrix} (\delta Q)_1 \\ (\delta V)_1 \\ (\delta G)_1 \\ (\delta F)_2 \\ (\delta Q)_2 \\ (\delta V)_2 \\ (\delta H)_2 \end{bmatrix}$$

$$+ \begin{bmatrix} -h/2 & 0 & 0 & 1 & 0 & 0 & 0 \\ -1 & 0 & 0 & 0 & -h/2 & 0 & 0 \\ 0 & -1 & 0 & 0 & 0 & -h/2 & 0 \\ 0 & 0 & -1 & 0 & 0 & 0 & -h/2 \\ (a_4)_S & (a_8)_S & (a_{12})_S & (a_1)_S & (a_5)_S & (a_9)_S & (a_{13})_S \\ (b_4)_S & (b_8)_S & (b_{12})_S & (b_1)_S & (b_5)_S & (b_9)_S & (b_{13})_S \\ (c_4)_S & (c_8)_S & (c_{12})_S & (c_1)_S & (c_5)_S & (c_9)_S & (c_{13})_S \end{bmatrix} \begin{bmatrix} (\delta P)_2 \\ (\delta \Theta)_2 \\ (\delta G)_2 \\ (\delta F)_3 \\ (\delta Q)_3 \\ (\delta V)_3 \\ (\delta H)_3 \end{bmatrix} = \begin{bmatrix} (r_1)_{S-\frac{1}{2}} \\ (r_2)_{S-\frac{1}{2}} \\ (r_3)_{S-\frac{1}{2}} \\ (r_4)_{S-\frac{1}{2}} \\ (r_5)_{S-\frac{1}{2}} \\ (r_6)_{S-\frac{1}{2}} \\ (r_7)_{S-\frac{1}{2}} \end{bmatrix}. \tag{6.72}$$

These results can be rewritten as follows

$$\begin{aligned} \text{for } s = 1: &\quad [A_2][\delta_2] + [C_2][\delta_3] = [r_1] \\ \text{for } s = 2: &\quad [B_3][\delta_2] + [A_3][\delta_3] + [C_3][\delta_4] = [r_2] \\ \text{for } s = 3: &\quad [B_4][\delta_2] + [A_4][\delta_3] + [C_4][\delta_4] = [r_3] \\ &\quad \vdots \\ \text{for } s = S-1: &\quad [B_{S-1}][\delta_{S-2}] + [A_{S-1}][\delta_{S-1}] + [C_{S-1}][\delta_S] = [r_{S-1}] \\ \text{for } s = S: &\quad [B_S][\delta_{S-1}] + [A_S][\delta_s] = [r_S] \end{aligned}$$

Lastly, the tridiagonal block matrix—the coefficient matrix—is obtained in linearized finite-difference equations. Formulas can be expressed as follows:

$$[A][\delta] = [r], \tag{6.73}$$

$$\begin{bmatrix} [A_2] & [C_2] & 0 & 0 & \dots & 0 \\ [B_3] & [A_3] & [C_3] & 0 & \dots & 0 \\ 0 & [B_4] & [A_4] & [C_4] & \dots & \vdots \\ \vdots & \vdots & \ddots & \ddots & \ddots & 0 \\ 0 & 0 & 0 & [B_{S-1}] & [A_{S-1}] & [C_{S-1}] \\ 0 & 0 & \dots & 0 & [B_S] & [A_S] \end{bmatrix} \begin{bmatrix} [\delta_1] \\ [\delta_2] \\ [\delta_3] \\ \vdots \\ [\delta_{S-1}] \\ [\delta_S] \end{bmatrix} = \begin{bmatrix} [r_1] \\ [r_2] \\ [r_3] \\ \vdots \\ [r_{S-1}] \\ [r_S] \end{bmatrix}, \tag{6.74}$$

where the square matrices of order 7 for $3 \le s \le S$ are $[A_2]$, $[A_s]$, $[B_s]$, and $[C_s]$. Matrix extraction details are available here. Moreover,

$$[A_2] = \begin{bmatrix} 0 & 0 & 0 & 1 & 0 & 0 & 0 \\ -h/2 & 0 & 0 & 0 & -h/2 & 0 & 0 \\ 0 & -h/2 & 0 & 0 & 0 & -h/2 & 0 \\ 0 & 0 & -1 & 0 & 0 & 0 & -h/2 \\ (a_6)_2 & (a_{10})_2 & (a_{12})_2 & (a_1)_2 & (a_5)_2 & (a_9)_2 & (a_{13})_2 \\ (b_6)_2 & (b_{10})_2 & (b_{12})_2 & (b_1)_2 & (b_5)_2 & (b_9)_2 & (b_{13})_2 \\ (c_6)_2 & (c_{10})_2 & (c_{12})_2 & (c_1)_2 & (c_5)_2 & (c_9)_2 & (c_{13})_2 \end{bmatrix}, \tag{6.75}$$

$$[C_s] = \begin{bmatrix} -h/2 & 0 & 0 & 0 & 0 & 0 & 0 \\ 1 & 0 & 0 & 0 & 0 & 0 & 0 \\ 0 & 1 & 0 & 0 & 0 & 0 & 0 \\ 0 & 0 & 1 & 0 & 0 & 0 & 0 \\ (a_3)_s & (a_7)_s & (a_{11})_s & 0 & 0 & 0 & 0 \\ (b_3)_s & (b_7)_s & (b_{11})_s & 0 & 0 & 0 & 0 \\ (c_3)_s & (c_7)_s & (c_{11})_s & 0 & 0 & 0 & 0 \end{bmatrix}; \ 2 \le s \le S-1, \tag{6.76}$$

$$[A_s] = \begin{bmatrix} -h/2 & 0 & 0 & 1 & 0 & 0 & 0 \\ -1 & 0 & 0 & 0 & -h/2 & 0 & 0 \\ 0 & -1 & 0 & 0 & 0 & -h/2 & 0 \\ 0 & 0 & -1 & 0 & 0 & 0 & -h/2 \\ (a_4)_s & (a_8)_s & (a_{12})_s & (a_1)_s & (a_5)_s & (a_9)_s & (a_{13})_s \\ (b_4)_s & (b_8)_s & (b_{12})_s & (b_1)_s & (b_5)_s & (b_9)_s & (b_{13})_s \\ (c_4)_s & (c_8)_s & (c_{12})_s & (c_1)_s & (c_5)_s & (c_9)_s & (c_{13})_s \end{bmatrix}; \ 3 \le s \le S, \tag{6.77}$$

$$[B_s] = \begin{bmatrix} 0 & 0 & 0 & -1 & 0 & 0 & 0 \\ 0 & 0 & 0 & 0 & -h/2 & 0 & 0 \\ 0 & 0 & 0 & 0 & 0 & -h/2 & 0 \\ 0 & 0 & 0 & 0 & 0 & 0 & -h/2 \\ 0 & 0 & 0 & (a_2)_s & (a_6)_s & (a_{10})_s & (a_{14})_s \\ 0 & 0 & 0 & (b_2)_s & (b_6)_s & (b_{10})_s & (b_{14})_s \\ 0 & 0 & 0 & (c_2)_s & (c_6)_s & (c_{10})_s & (c_{14})_s \end{bmatrix}; \ 3 \le s \le S, \tag{6.78}$$

$$[\delta_2] = \begin{bmatrix} (\delta Q)_1 & (\delta V)_1 & (\delta G)_1 & (\delta F)_2 & (\delta Q)_2 & (\delta V)_2 & (\delta H)_2 \end{bmatrix}^T, \tag{6.79}$$

and

$$[\delta_s] = \begin{bmatrix} (\delta P)_{s-1} & (\delta \Theta)_{s-1} & (\delta G)_{s-1} & (\delta F)_s & (\delta Q)_s & (\delta V)_s & (\delta H)_s \end{bmatrix}^T, \quad 3 \le s \le S. \tag{6.80}$$

Similarly

$$[r_s] = \begin{bmatrix}(r_1)_{s-\frac{1}{2}} & (r_2)_{s-\frac{1}{2}} & (r_3)_{s-\frac{1}{2}} & (r_4)_{s-\frac{1}{2}} & (r_5)_{s-\frac{1}{2}} & (r_6)_{s-\frac{1}{2}} & (r_7)_{s-\frac{1}{2}}\end{bmatrix}^T, \tag{6.81}$$

We assume that A is non-singular and may be factored as follows in order to continue:

$$[A] = [L][U], \tag{6.82}$$

in which

$$[L] = \begin{bmatrix}[\alpha_2] & 0 & 0 & 0 & \dots & 0 \\ [\beta_3] & [\alpha_3] & 0 & 0 & \dots & 0 \\ 0 & [\beta_4] & [\alpha_4] & 0 & \dots & \vdots \\ \vdots & \vdots & \ddots & \ddots & \ddots & 0 \\ 0 & 0 & 0 & [\beta_{S-1}] & [\alpha_{S-1}] & 0 \\ 0 & 0 & \dots & 0 & [\beta_S] & [\alpha_S]\end{bmatrix}, \tag{6.83}$$

and

$$[U] = \begin{bmatrix}[I] & [\Gamma_1] & 0 & 0 & \dots & 0 \\ 0 & [I] & [\Gamma_2] & 0 & \dots & 0 \\ 0 & 0 & [I] & [\Gamma_3] & \dots & \vdots \\ \vdots & \vdots & \ddots & \ddots & \ddots & 0 \\ 0 & 0 & 0 & 0 & [I] & [\Gamma_{S-1}] \\ 0 & 0 & \dots & 0 & 0 & [I]\end{bmatrix}, \tag{6.84}$$

The following equations define the elements of the preceding formula, where $[I]$ is a matrix of order 7, $[\alpha_i]$, and $[\Gamma_i]$ are 7×7 matrices.

$$[\alpha_2] = [A_2], \tag{6.85}$$

$$[A_2][\Gamma_2] = [C_2], \tag{6.86}$$

$$[\alpha_s] = [A_s] - [B_s][\Gamma_{s-1}], \quad s = 3, 4, ..., S \tag{6.87}$$

$$[\alpha_s][\Gamma_s] = [C_s], \quad s = 3, 4, ..., S-1. \tag{6.88}$$

By invoking Eq. (6.82) into Eq. (6.73), we arrived at

$$[L][U][\delta] = [r], \tag{6.89}$$

Next, by defining $[U][\delta] = [W]$, Eq. (6.89) can be expressed as

$$[L][W] = [r]. \tag{6.90}$$

where

$$[W] = \begin{bmatrix}[W_2] & [W_3] & \cdots & [W_{S-1}] & [W_S]\end{bmatrix}^T, \quad 2 \le s \le S, \tag{6.91}$$

and $[W_s]$ are matrices with 7×1 columns. Eq. (6.92) can be used to solve the elements of matrix W, and their mathematical expression is

$$[\alpha_2][W_2] = [r_1], \tag{6.92}$$

$$[\alpha_s][W_s] = [r_s] - [B_s][W_{s-1}] \quad 3 \le s \le S. \tag{6.93}$$

Forward sweep is used to determine Γ_s, α_s, and W_s. The solution, known as the "backward sweep," is provided by $[U][\delta] = [W]$, once the elements of W have been located. The elements are derived using the following relations:

$$[\delta_S] = [W_S], \tag{6.94}$$

$$[\delta_s] = [W_s] - [\Gamma_s][\delta_{s+1}], \quad 2 \le s \le S-1. \tag{6.95}$$

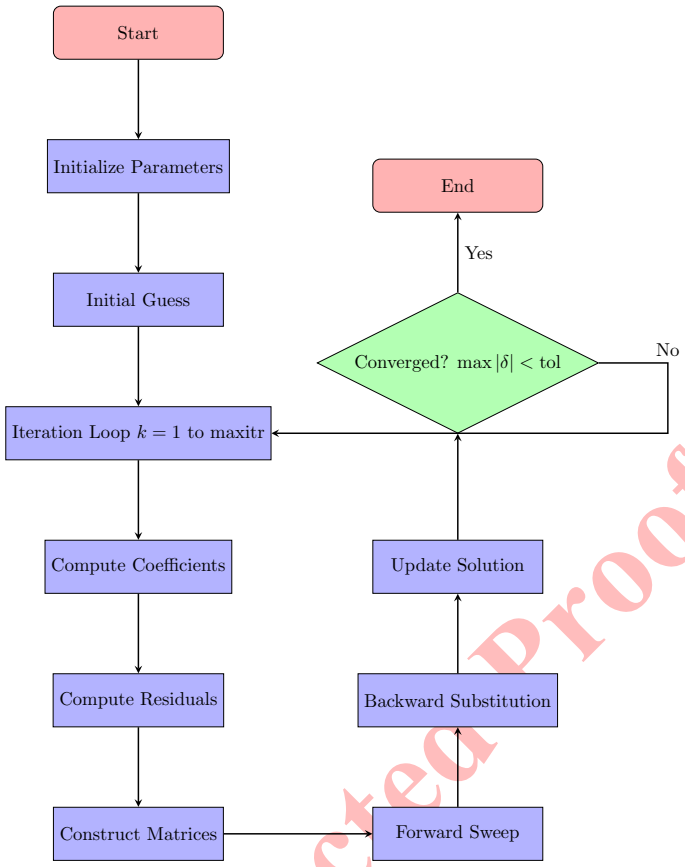

FIGURE 4. Flowchart of the Keller-Box method.

These calculations are repeated until some convergence criterion is satisfied and calculations are stopped when

$$|\delta Q_1^{(i)}| \leq \epsilon_1, \tag{6.96}$$

where $\epsilon_1 = 10^{-4}$ is small prescribed value.

In this work, LU decomposition was selected for solving the block-tridiagonal system arising from the Keller Box discretization. The main reason is that LU factorization is computationally less expensive than orthogonal factorizations (such as QR or Householder methods) when dealing with large but structured systems, like those produced by finite-difference schemes. The Keller Box Method naturally leads to a sparse and banded matrix structure, for which LU decomposition provides an efficient and straightforward solution strategy without excessive memory requirements.

Although orthogonal factorizations generally offer superior numerical stability, the block-tridiagonal structure in this case is well-conditioned, and stability can be maintained with proper grid refinement and step-size control. Thus, LU decomposition achieves a balance between accuracy and computational efficiency, making it well-suited for iterative schemes within boundary-layer flow problems. A brief exploration of alternative factorizations, such as QR, could be considered in future work for cases where ill-conditioning becomes significant.

The detailed KBM algorithm of the present problem is given in Figure 4 and Algorithm 1.

Algorithm 1 KBM Algorithm.

Initialize:
$h := 0.01$, $\eta_0 := 0$, $\eta_f := 7$
Set Physical Parameters:
$(We, n, m, Gr, M, Rd, \theta_w, Pr, Nt, Nb, \gamma, \eta, Sca, K, \Lambda, \chi)$
Initial solution vector:

$$F_1 := \chi\frac{1-m}{m+1}, \quad P_1 := 1, \quad Q_1 := 0, \quad \Theta_1 := 1, \quad V_1 := 0, \quad G_1 := 0, \quad H_1 := \Lambda G_1$$
$$F_1 := 0, \quad P_1 := 0, \quad Q_1 := 0, \quad \Theta_1 := 0, \quad V_1 := 0, \quad G_1 := 0, \quad H_1 := 0 \quad (i = 2, \ldots, N)$$
$$F_{N+1} := 0, \quad P_{N+1} := 0, \quad Q_{N+1} := 0, \quad \Theta_{N+1} := 0, \quad V_{N+1} := 0, \quad G_{N+1} := 1, \quad H_{N+1} := 0$$

Iteration loop:
for $k := 1$ to maxitr (1000) **do**
  for $j := 2$ to $N + 1$ **do**
    Compute coefficients $ai_{1,j}$ to $ai_{14,j}$, $bi_{1,j}$ to $bi_{14,j}$, $ci_{1,j}$ to $ci_{14,j}$
    Compute residuals $r_{1,j}$ to $r_{7,j}$
  end for
  Construct matrices:
  Build A_1, C_1, R_1
  for $j := 2$ to N **do**
    Build A_j, B_j, C_j, R_j
  end for
  Build A_{N+1}, B_{N+1}, R_{N+1}
  Block elimination:
  $\alpha_1 := A_1$, $\gamma_1 := A_1^{-1}C_1$
  for $i := 2$ to N **do**
    $\alpha_i := A_i - B_i\gamma_{i-1}$, $\gamma_i := \alpha_i^{-1}C_i$
  end for
  $\alpha_{N+1} := A_{N+1} - B_{N+1}\gamma_N$
  Backward substitution:
  $W_1 := \alpha_1^{-1}R_1$
  for $i := 2$ to $N + 1$ **do**
    $W_i := \alpha_i^{-1}(R_i - B_iW_{i-1})$
  end for
  $\delta_{N+1} := W_{N+1}$
  for $i := N$ down to 1 **do**
    $\delta_i := W_i - \gamma_i\delta_{i+1}$
  end for
  Update solution:
  for $i := 1$ to $N + 1$ **do**
    $F_i := F_i + \delta F_i$, $P_i := P_i + \delta P_i$, $Q_i := Q_i + \delta Q_i$, $\Theta_i := \Theta_i + \delta\Theta_i$, $V_i := V_i + \delta V_i$, $G_i := G_i + \delta G_i$, $H_i := H_i + \delta H_i$
  end for
  Check convergence:
  $\delta_{\max} := \max(|\delta F|, |\delta P|, |\delta Q|, |\delta\Theta|, |\delta V|, |\delta G|, |\delta H|)$
  if $\delta_{\max} <$ tol (10^{-10}) **then**
    Break iteration loop
  else
    Update initial guesses with current solution
  end if
end for

TABLE 2. The values of $C_{f_x}Re_x^{\frac{1}{2}}$ when $Pr = 6.8$, $Rd = 1$, $Nb = 0.1$, $Nt = 0.1$, $\gamma = 0.09$, $We = 0.1$, $Gr = 1$, $\theta_w = 1.2$, $Sc = 0.62$, $K = 0.1$, $\Lambda = 0.3$, $\chi = 0.1$.

n	m	We	Gr	M	KBM	CPU (sec)
0.2	0.4	0.1	1	2	-0.0060	0.4716
0.4					-0.0015	0.5078
0.6					-2.9952	0.4739
0.7					-1.2427	36.1964
	0.5				-0.0059	0.5523
	0.7				-0.0056	0.5217
	0.9				-0.0054	0.5386
		0.3			-0.0061	0.7689
		0.5			-0.0061	0.4874
		0.8			-0.0062	0.7214
			2		-0.0083	0.5744
			4		-0.0105	0.5952
			6		-0.0116	0.5243
				4	-0.0052	0.5166
				7	-0.0043	0.4696
				9	-0.0040	0.5127

7. Computational results analysis for momentum, energy, and homogeneous-heterogeneous equations

This section presents the numerical results for momentum, energy, and homogeneous-heterogeneous equations in tangent hyperbolic fluid flow over the upper surface of a paraboloid of revolution. The data, shown through tables and graphs, were obtained by varying key physical quantities in the Ordinary Differential Equations (ODEs). The influence of dimensionless parameters on the skin friction coefficient $C_{f_x}Re_x^{\frac{1}{2}}$ and nusselt number $Nu_xRe_x^{-\frac{1}{2}}$ is analyzed in detail using various graphs and tables. Specifically, Tables 2 and 3 examine the impact of parameters like Radiation (Rd), Brownian motion (Nb), Thermophoresis (Nt), Internal heat source (γ), Weissenberg number (We), Grashof number (Gr), Temperature parameter (θ_w), Diffusion rate ratio (Sc), Homogeneous reaction strength (K), Heterogeneous reaction strength (Λ), and Similarity variable (ς) on fluid motion and temperature fluctuations, with $Pr = 6.8$ fixed. Default values for parameters were: $Rd = 1$, $Nb = 0.1$, $Nt = 0.1$, $\gamma = 0.09$, $We = 0.1$, $Gr = 1$, $\theta_w = 1.2$, $Sc = 0.62$, $K = 0.1$, $\Lambda = 0.3$, and $\chi = 0.1$. Due to the impracticality of solving over an infinite interval, a finite point of $\varsigma = 7$ was used to approximate the boundary condition.

8. Verification of the results

To confirm the precision of this analysis, the outcomes under the specified conditions ($Pr = 6.8$, $Rd = 1$, $Nb = 0.1$, $Nt = 0.1$, $\gamma = 0.09$, $We = 0.1$, $n = 0.2$, $m = 0.4$, $Gr = 1$, $\theta_w = 1.2$, $Sc = 0.62$, $K = 0.1$, $A = 0.3$, and $\chi = 0.1$) show strong agreement with the Computational Grid Validation Results presented in Table 4. Examining this table, we observe that as the step size (h) decreases, the number of nodes increases, and the value of $F(\zeta = 7)$ converges towards a consistent result. This convergence indicates that the solution becomes largely independent of h as it is reduced, with further reductions yielding insignificant changes in the $F(\zeta = 7)$ values.

For the validation of the developed MATLAB code, the present skin friction results are examined under the limiting case and compared with the previously published findings of [3, 22], and [8]. As presented in Table 5, the numerical values demonstrate an excellent level of consistency with the cited studies.

TABLE 3. The values of $Nu_x Re_x^{\frac{-1}{2}}$ when $Pr = 6.8$, $We = 0.1$, $Gr = 1$, $M = 2$, $Sc = 0.62$, $K = 0.1$, $\Lambda = 0.3$, $\chi = 0.1$, $\theta_w = 1.2$.

Rd	n	Nb	Nt	γ	m	KBM	CPU (sec)
1	0.2	0.1	0.1	0.09	0.4	0.0873	0.4827
2						0.1311	0.4963
4						0.2222	0.4602
6						0.3512	0.4209
	0.3					0.0503	0.4624
	0.5					0.0152	0.5037
	0.7					0.0046	2.4453
		0.5				0.0874	0.4880
		2				0.0877	0.5117
		3				0.0879	2.8220
			0.2			0.0873	1.2382
			0.3			0.0872	0.6295
			0.6			0.0871	0.6767
				0.01		0.0125	0.5005
				0.03		0.0345	0.4806
				0.05		0.0539	0.5036
					0.6	0.0760	0.5551
					0.8	0.0672	0.5555
					0.9	0.0635	0.5703

TABLE 4. Computational grid validation results.

h	Nodes	$F(\varsigma = 7)$	Iterations
0.014	501	0.854169	40
0.007	1001	0.854167	40
0.0035	20001	0.854166	40
0.0028	2501	0.854166	40
0.0023	3501	0.854166	40

TABLE 5. Numerical comparison of skin friction coefficient.

M	[3]	[22]	[8]	Current study
0	-1	-1	-1	-1
1	-1.41421	-1.41419	-1.414214	-1.41421
5	-2.449449	-2.44945	-2.449490	-2.44948
10	-3.31663	-3.31657	-3.316625	-3.31662
100	-10.0498	-10.04981	-10.049876	-10.04987
500	-22.38303	-22.38294	-21.478413	-21.47840
1000	-31.63859	-31.63851	-31.63819	-31.63849

9. GRAPHICAL SIMULATIONS

Figure 5 illustrates the relationship between the magnetic parameter (M) and the Nusselt number (Nu), a measure of convective heat transfer efficiency. The bars show that as the magnetic parameter increases from 1 to 4, the Nusselt number also consistently rises from approximately 0.0692 to 0.1159. This indicates a direct positive correlation,

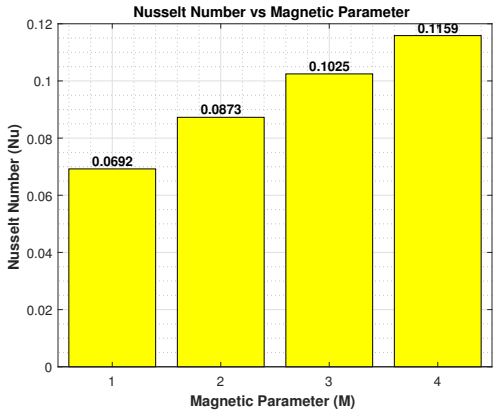

FIGURE 5. Variation in Nusselt number with change in magnetic parameter.

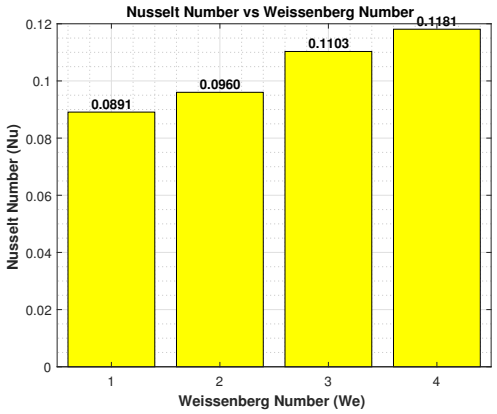

FIGURE 6. Variation in Nusselt number with change in Weissenberg number.

suggesting that a stronger magnetic field enhances heat transfer in this specific system, possibly by inducing fluid instabilities or secondary flows that improve mixing and disrupt thermal boundary layers. The numerical values atop each bar provide precise Nusselt number readings for each corresponding magnetic parameter value, quantifying the degree of heat transfer enhancement with increasing magnetic field strength.

Figure 6 demonstrates a clear positive correlation between the Weissenberg number (We), indicative of fluid elasticity, and the Nusselt number (Nu), a measure of convective heat transfer efficiency. As We increases from 1 to 4, Nu correspondingly rises from 0.0891 to 0.1181, as reflected in both bar heights and annotated values. This trend suggests that enhanced fluid elasticity augments internal mixing and advective transport, thereby facilitating more effective thermal energy transfer. Thus, increased elastic behavior in the fluid markedly improves heat transfer performance in the system.

Figure 7 illustrating the effect of the power-law index (n) on the velocity profile $F'(\varsigma)$, we can observe a clear trend: as the value of n increases from 0.2 to 0.7, the fluid velocity decreases across the entire domain (ς). For the smallest value of $n = 0.2$, the velocity is highest, and progressively lower velocities are observed for $n = 0.4$, $n = 0.6$, and $n = 0.7$. This aligns with the provided note stating that velocity estimation reduces as n improves. Higher values of n generally correspond to a more shear-thinning behavior, where the apparent viscosity of the fluid decreases with increasing shear rate.

Figure 8 depicts the influence of the Weissenberg number (We) on the fluid velocity profile $F'(\varsigma)$. As a dimensionless parameter quantifying the ratio of relaxation time to characteristic flow time, We reflects the fluid's elastic response to deformation. An increase in We signifies a stronger dominance of elastic over viscous forces, indicative of enhanced non-Newtonian behavior. The figure reveals that as We rises from 0.1 to 0.8, the velocity profile $F'(\varsigma)$ consistently declines throughout the domain, implying that greater elasticity suppresses flow velocity.

Figure 9 compellingly demonstrates the influence of the thermal Grashof number, Gr, on horizontal velocity, $F'(\varsigma)$. As Gr increases ($Gr = 1, 2, 4, 6$), the velocity near the surface ($\varsigma = 0$) notably intensifies. Physically, this aligns with the definition of Gr—the ratio of buoyant to viscous forces. Elevated Gr implies dominant buoyancy due to thermal gradients, which diminishes viscous resistance and enhances horizontal flow near the surface. The graph clearly visualizes this velocity augmentation with rising Gr.

Figure 10 illustrates the impact of the magnetic parameter M on the fluid velocity $F'(\varsigma)$. As M increases (from 2 to 9), the velocity profiles shift downward, indicating a clear reduction in fluid speed. Additionally, the boundary layer—where velocity deviates from zero—thins with higher M. This behavior stems from the Lorentz force induced in an electrically conducting fluid under a magnetic field. Since M represents the ratio of magnetic to viscous forces,

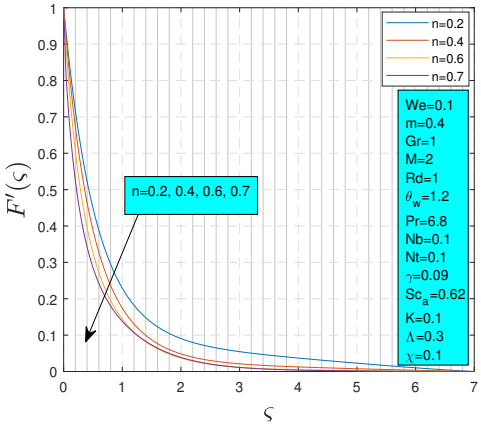

FIGURE 7. Effect of n on $F'(\varsigma)$.

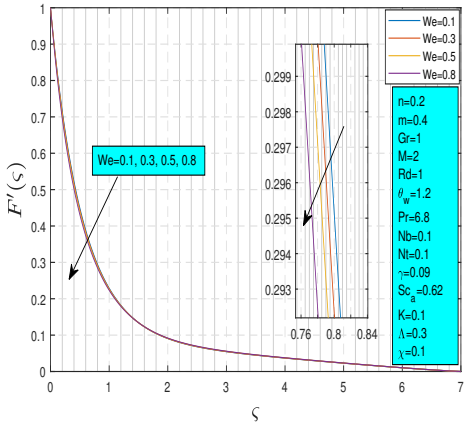

FIGURE 8. Effect of We on $F'(\varsigma)$.

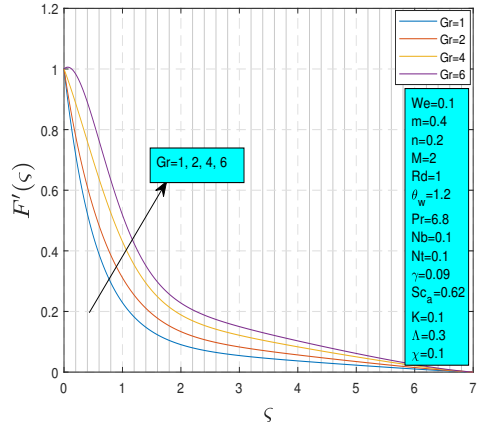

FIGURE 9. Effect of Gr on $F'(\varsigma)$.

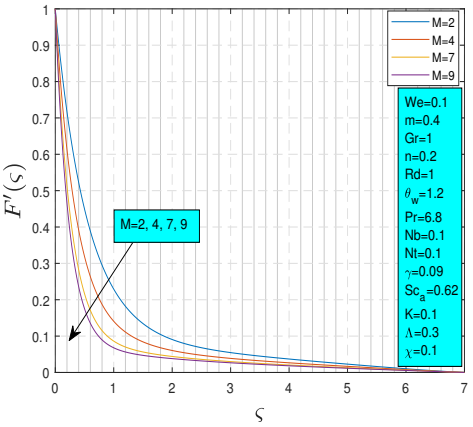

FIGURE 10. Effect of M on $F'(\varsigma)$.

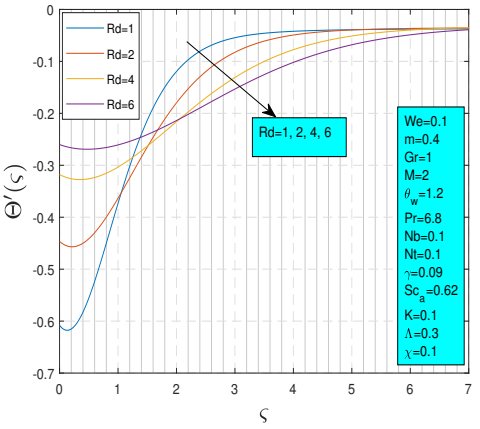

FIGURE 11. Effect of Rd on $\Theta'(\varsigma)$.

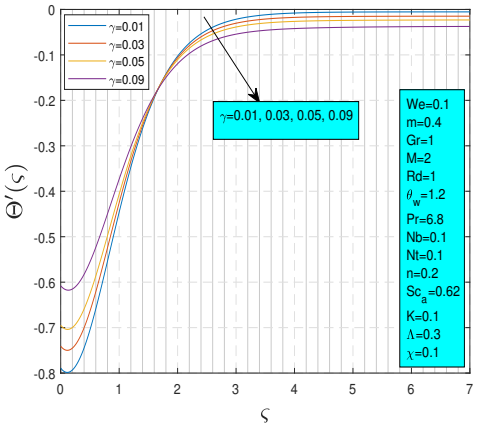

FIGURE 12. Effect of γ on $\Theta'(\varsigma)$.

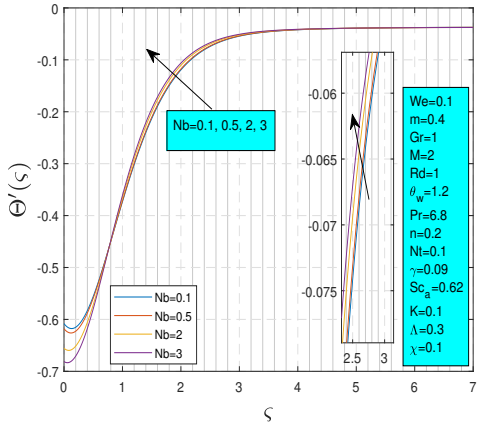

FIGURE 13. Effect of Nb on $\Theta'(\varsigma)$.

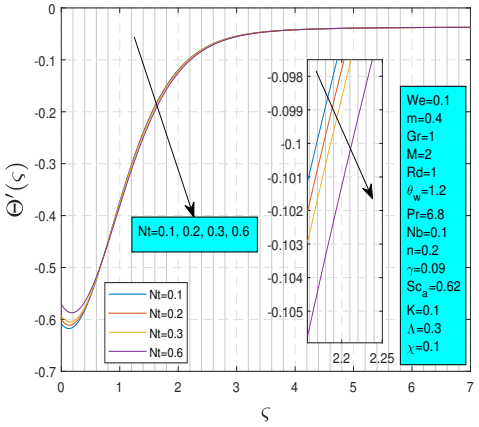

FIGURE 14. Effect of Nt on $\Theta'(\varsigma)$.

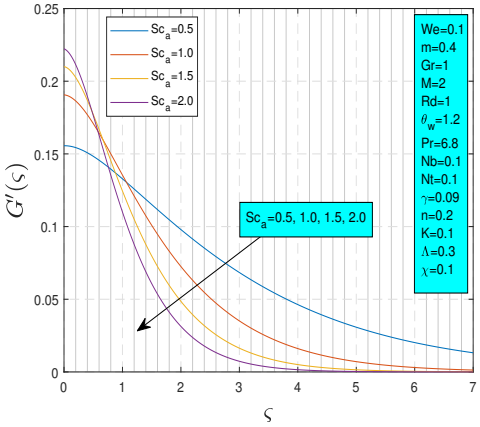

FIGURE 15. Effect of Sc_a on $G'(\varsigma)$.

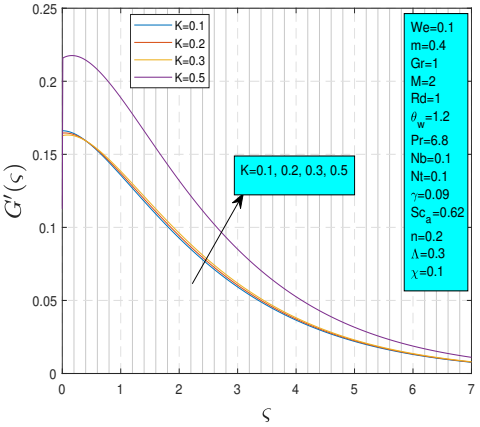

FIGURE 16. Effect of K on $G'(\varsigma)$.

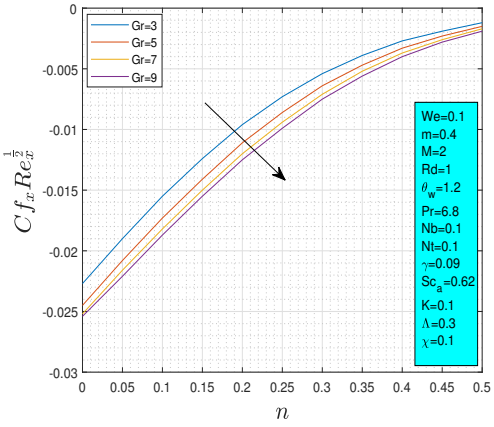

FIGURE 17. Skin friction coefficients vs n for various values of Gr.

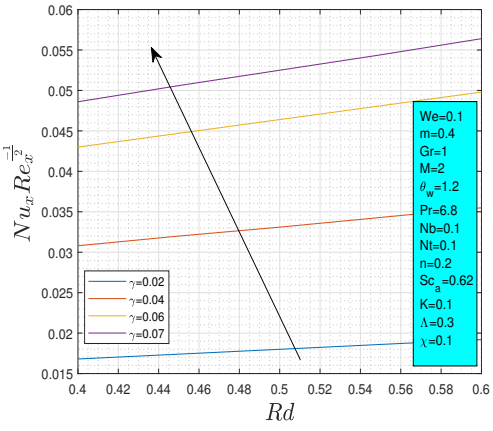

FIGURE 18. Local Nusselt number vs Rd for various values of γ.

a larger M intensifies this opposing (retarding) force, thereby suppressing the fluid motion throughout the boundary layer.

Figure 11 illustrates the impact of Thermal Radiation (Rd) on the temperature profile $\Theta'(\varsigma)$. Thermal radiation is the energy emitted by matter as electromagnetic waves due to its temperature. As the value of Thermal Radiation (Rd) increases, we can clearly observe from the graph that the temperature profile $\Theta'(\varsigma)$ decreases across the domain ς. Specifically, the curves for higher values of Rd (like $Rd = 4$ and $Rd = 6$) lie below the curves for lower values ($Rd = 1$ and $Rd = 2$). This decrease in temperature profile with increasing thermal radiation can be attributed to the fact that a higher Rd signifies a greater contribution of radiative heat transfer.

Referring to Figure 12, which depicts the influence of the space-dependent internal heat source parameter (γ) on the temperature gradient $\Theta'(\varsigma)$, we observe distinct behavior near and far from the wall. Near the wall (ς small), as γ increases (from 0.01 to 0.09), the temperature gradient steepens, signaling a heightened rate of heat transfer. However, farther from the wall (ς large), the trend reverses, with the temperature gradient becoming less steep as γ rises, indicating a reduced heat transfer rate. The graph conclusively shows that as γ increases (0.01, 0.03, 0.05, 0.09), the overall temperature profile $\Theta(\varsigma)$ diminishes.

Figure 13 elucidates the influence exerted by the Brownian motion parameter (Nb) on the temperature gradient $\Theta'(\varsigma)$. As the value of Nb ascends (ranging from 0.1 to 3), the intensity of the negative temperature gradient proximate to the surface ($\varsigma = 0$) diminishes, signifying a decrement in the rate of heat transfer. This phenomenon arises due to the facilitative impact of Brownian motion in augmenting thermal conductivity by fostering the movement of nanoparticles. While this enhancement bolsters the fluid's overall heat transfer capability, it concurrently fosters a more homogenized temperature distribution close to the surface, thereby attenuating the temperature gradient and, as a result, diminishing the local heat transfer rate.

The Figure 14 shows that as the thermophoresis parameter (Nt) increases, the temperature profile $\Theta'(\varsigma)$ decreases. This happens because a higher Nt signifies a stronger thermophoretic force, which causes more suspended particles to move from hotter regions to colder regions. Assuming heat transfer from a surface, the area near the surface is hotter, and with increased Nt, more heated particles are driven away from this surface towards the cooler fluid. This migration of thermal energy carried by the particles results in a reduction of the temperature profile in the vicinity of the heat source, explaining the inverse relationship observed in the graph.

Figure 15 a keen observation about how the Schmidt number (Sc_a) affects those concentration profile in the graph. The graph visually confirms this. As we move from the blue line ($Sc_a = 0.5$) to the purple line ($Sc_a = 2.0$), the curves become steeper near $\varsigma = 0$ and decay more rapidly, indicating a thinner concentration boundary layer. This implies that for both types of reactions happening at or within the fluid, a larger Sc_a hinders the spread of the reactant, leading to lower concentration values as you move away from the reacting surface or source. So, the reason the profiles decrease with increasing Sc_a in the graph is a direct consequence of the reduced mass diffusion relative to momentum diffusion.

The Figure 16 illustrates the impact of the strength of the homogeneous reaction, denoted by K, on the homogeneous-heterogeneous profile $G'(\varsigma)$. The definition of the strength of homogeneous reaction relates to the rate at which a reaction occurs uniformly within a single phase of a system. Observing the figure, as the value of K increases from 0.1 to 0.5, the curves for $G'(\varsigma)$ show a noticeable increase across the entire domain of ς. This indicates that a stronger homogeneous reaction leads to a higher concentration or activity within the system's bulk. Essentially, with a larger K, the bulk of the fluid becomes more concentrated in the reacting species, which elevates the entire $G'(\varsigma)$ profile. The other parameters (We=0.1, m=0.4, Gr=1, M=2, Rd=1, θ_w=1.2, Pr=6.8, Nb=0.1, Nt=0.1, γ=0.09, Sc_a=0.62, n=0.2, Λ=0.3, ς=0.1) are held constant in this specific analysis, allowing us to isolate and observe the sole impact of the strength of the homogeneous reaction K.

Figure 17 shows how the skin friction coefficient, $C_{f_x} Re_x^{1/2}$, varies with the power-law index (n) for different Grashof numbers (Gr). As Gr increases (from 3 to 9), the skin friction coefficient decreases. Higher Gr values indicate stronger buoyancy forces, which enhance convection and alter velocity gradients near the surface. The power-law index (n) defines the fluid's behavior: for $n < 1$, the fluid is shear-thinning, for $n > 1$, it's shear-thickening, and for $n = 1$, it's Newtonian. This decrease in skin friction with increasing Gr suggests that stronger buoyancy-driven flows reduce surface friction.

Figure 18, shows as the Space dependent internal heat source parameter (γ) increases (from the blue line at $\gamma = 0.02$ to the purple line at $\gamma = 0.07$), the coefficient of the local Nusselt number ($Nu_x Re_x^{\frac{-1}{2}}$) also increases for any given value of the thermal radiation parameter (Rd). This increasing trend is visually represented by the upward shift of the lines corresponding to higher γ values. Consequently, as γ increases, the local Nusselt number coefficient also increases, indicating more effective convective cooling or heating at the surface. Regarding the thermal radiation parameter (Rd), the graph shows that for a fixed value of γ, as Rd increases (moving along any single colored line from left to right), there is a slight increase in the local Nusselt number coefficient.

10. Conclusion

The analysis demonstrates the influence of dimensionless parameters on non-Newtonian fluid flow under magnetic fields, thermal radiation, internal heat generation, and chemical reactions, affecting velocity, temperature, concentration, and heat transfer. Key findings include:

- Increasing M enhances heat transfer (Nu) but reduces velocity and thins the velocity boundary layer.
- Higher We improves heat transfer, showing beneficial elastic effects.
- Larger n lowers velocity, reflecting shear-thinning behavior.
- Increased Gr accelerates horizontal fluid motion via stronger buoyancy.
- Higher Rd reduces temperature due to radiative losses.
- Internal heat generation (γ) slightly raises the local Nusselt number.
- Stronger Nb flattens the temperature gradient near the surface, decreasing local heat transfer.
- Higher Sc_a thins concentration boundary layers, limiting mass diffusion.
- Increased K enhances homogeneous-heterogeneous reaction profiles.

Future studies may explore varying surface geometries, additional physical effects (e.g., Joule heating, space-dependent thermal radiation, slip conditions), numerical stability, and machine learning-based predictions to further understand tangent hyperbolic fluid behavior.

Nomenclature.

θ_w	Temperature parameter	n	Power law index
ν	Kinematic viscosity	τ	Dimensionless time
We	Weissenberg number	C_f	Skin friction coefficient
τ_w	Wall shear stress	k	Thermal conductivity
α	Thermal diffusivity	m	Velocity power index
u	$\bar{x}$-component of fluid velocity	v	$\bar{y}$-component of fluid velocity
Gr	Grashof number	B	Inclined magnetic field
B_0	Magnetic field constant	ρC_p	Heat capacity
b	Stretching sheet parameter	K_1, K_s	Reaction rate coefficient
T_∞	Ambient temperature	T	Fluid temperature
q_r	Radiative heat flux	q_w	Heat flux
$\sigma^\star$	Stefan Boltzmann constant	$k^\star$	Absorption coefficient
ψ	Stream function	θ	Stream function
η	Similarity variable	Nt	Thermophoresis parameter
Nb	Brownian motion parameter	Rd	Radiation parameter
K	Strength of homogeneous reaction	γ	Space dependent internal heat source parameter
Λ	Strength of heterogeneous reaction	Nu	Nusselt number
δ	Ratio of diffusion coefficients chemical reactant A to reactant B	M	Magnetic parameter
Sc_a	Ratio of viscous diffusion rate to mass diffusion rate of reactant A	Re_x	Reynolds number
Sc_b	Ratio of viscous diffusion rate to mass diffusion rate of specie B	Pr	Prandtl number

Acknowledgment

I would like to express my sincere gratitude to the University of Tabriz and to the journal Computational Methods for Differential Equations (CMDE) for providing a highly supportive and innovative research environment that enabled the successful publication of our work. We are particularly appreciative that CMDE is indexed in well-recognized

databases such as Web of Science, Scopus, Clarivate Analytics (ESCI), ISC (Islamic World Science Citation Center), Zentralblatt, and DOAJ, which reflects the journal's high academic standards and global impact. On behalf of all the authors, I deeply acknowledge and appreciate the dedicated efforts and professionalism of the entire editorial and journal team.

I am also sincerely grateful to all my co-authors for their active participation, valuable discussions, and strong commitment throughout the research process. In particular, I would like to express my special appreciation to Habiba Niaz, who comes from the beautiful region of Abbaspur City, Kashmir. Her continuous motivation, positive attitude, and efforts to create a productive and collaborative discussion environment played a significant role in the completion of this work. As the first author, I truly acknowledge and value her contributions and dedication.

We hope that our collective efforts will contribute meaningfully to future research and inspire further exploration within this specialized domain.

Authors Contribution

*__Atif Ali Zafar__:- Methodology, Investigation, Validation, Project supervision, Writing-original draft.
__Habiba Niaz__:- Conceptualization, Investigation, Reviewing original draft.
__Hadia Parveen__:- Formal analysis, Visualization.

References

[1] O. A. Abegunrin, S. O. Okhuevbie, and I. L. Animasaun, *Comparison between the flow of two non-Newtonian fluids over an upper horizontal surface of paraboloid of revolution: Boundary layer analysis*, Alexandria Eng. J., *55* (2016), 1915–1929.

[2] R. P. Agarwal, A. M. Alghamdi, S. Gala, and M. A. Ragusa, *On the regularity for weak solutions to the micropolar fluid flows*, Appl. Comput. Math., *23* (2024), 558–569.

[3] N. S. Akbar, A. Ebaid, and Z. H. Khan, *Numerical analysis of magnetic field effects on Eyring-Powell fluid flow towards a stretching sheet*, J. Magn. Magn. Mater., *382* (2015), 355–358.

[4] M. M. AlBaidani, M. M. A. Lashin, R. S. Saif, and A. H. Ganie, *Homogeneous–heterogeneous reactions for Maxwell nanofluid flow over an elongating cylindrical pipe via finite element method*, ZAMM Z. Angew. Math. Mech., *103* (2023), e202100386.

[5] I. L. Animasaun, *Effects of thermophoresis, variable viscosity and thermal conductivity on free convective heat and mass transfer of non-darcian MHD dissipative Casson fluid flow with suction and nth order of chemical reaction*, J. Niger. Math. Soc., *34* (2015), 11–31.

[6] I. L. Animasaun, C.S.K. Raju, and N. Sandeep, *Unequal diffusivities case of homogeneous–heterogeneous reactions within viscoelastic fluid flow in the presence of induced magnetic-field and nonlinear thermal radiation*, Alexandria Eng. J., *55* (2016), 1595–1606.

[7] K. K. Asogwa, B. S. Goud, N. A. Shah, and S. J. Yook, *Rheology of electromagnetohydrodynamic tangent hyperbolic nanofluid over a stretching riga surface featuring dufour effect and activation energy*, Sci. Rep., *12* (2022), 14602.

[8] S.M. Atif, W.A. Khan, M. Abbas, and U. Rashid, *Bioconvection mangnetohydrodynamic tangent hyperbolic nanofluid flow with quartic chemical reaction past a paraboloid surface*, Comput. Model. Eng. Sci., *130* (2022), 205–20.

[9] W. Cao, S. U. Rehman, and M. I. Asjad, *NUMERICAL STUDY OF BIOCONVECTION AND CATTANEO-CHRISTOV HEAT FLUX MODEL IN MHD MAXWELL NANOFLUID FLOW OVER A VARIABLE THICKNESS ELASTIC SURFACE*, Appl. Comput. Math., *23* (2024), 182—200.

[10] T. Cebeci and P. Bradshaw, *Momentum transfer in boundary layers*, Washington, (1977).

[11] M. A. Chaudhary and J. H. Merkin, *A simple isothermal model for homogeneous-heterogeneous reactions in boundary-layer flow. I Equal diffusivities*, Fluid Dyn. Res., *16* (1995), 311–333.

[12] S. Abdul Gaffar, O. A. Bég, T. A. Bég, S. Kuharat, and P. Ramesh Reddy, *Analysis of External Magnetized Dissipative Thermo-convective Tangent Hyperbolic-micropolar Flow on a Rotating Non-isothermal Cone with Hall Current and Joule Dissipation: Electro-conductive Polymer Spin Coating*, J. Appl. Comput. Mech., *11* (2025), 1039-1059.

[13] R. Hu and A. V. Sapre, *Analysis of autocatalytic reactions in isothermal catalyst particles*, AIChE J., *36* (1990), 342–352.
[14] F. Hussain, A. Hussain, and S. Nadeem, *Thermophoresis and Brownian model of pseudo-plastic nanofluid flow over a vertical slender cylinder*, Math. Probl. Eng., *2020* (2020), 8428762.
[15] H. B. Keller and T. Cebeci, *Accurate numerical methods for boundary-layer flows. II: Two dimensional turbulent flows*, AIAA J., *10* (1972), 1193–1199.
[16] Y. G. Kim, *Some properties of autocatalytic reactions*, Chem. Eng. Sci., *23* (1968), 687–694.
[17] O. K. Koriko, A. J. Omowaye, N. Sandeep, and I. L. Animasaun, *Analysis of boundary layer formed on an upper horizontal surface of a paraboloid of revolution within nanofluid flow in the presence of thermophoresis and Brownian motion of 29 nm CuO*, Int. J. Mech. Sci., *124* (2017), 22–36.
[18] Y. Kumar and S. Pandit, *Haar wavelet analysis of axisymmetric vibration of 2-D functionally graded porous thin annular plate resting on the Winkler foundation*, Eng. Comput., *42* (2025), 205–233.
[19] D. T. Lynch, *Chaotic behavior of reaction systems: mixed cubic and quadratic autocatalysis*, Chem. Eng. Sci., *47* (1992), 4435–4444.
[20] O. D. Makinde and I. L. Animasaun, *Bioconvection in MHD nanofluid flow with nonlinear thermal radiation and quartic autocatalysis chemical reaction past an upper surface of a paraboloid of revolution*, Int. J. Therm. Sci., *109* (2016), 159–171.
[21] O. D. Makinde and I. L. Animasaun, *Thermophoresis and Brownian motion effects on MHD bioconvection of nanofluid with nonlinear thermal radiation and quartic chemical reaction past an upper horizontal surface of a paraboloid of revolution*, J. Mol. Liq., *221* (2016), 733–743.
[22] M. Y. Malik, T. Salahuddin, A. Hussain, and S. Bilal, *MHD flow of tangent hyperbolic fluid over a stretching cylinder: using Keller box method*, J. Magn. Magn. Mater., *395* (2015), 271–276.
[23] A. Malvandi, S. Heysiattalab, and D. D. Ganji, *Thermophoresis and Brownian motion effects on heat transfer enhancement at film boiling of nanofluids over a vertical cylinder*, J. Mol. Liq., *216* (2016), 503–509.
[24] M. H. Matin, O. Mahian, and S. Wongwises, *Nanofluids flow between two rotating cylinders: effects of thermophoresis and brownian motion*, J. Thermophys. Heat Transfer, *27* (2013), 748–755.
[25] R. C. Mittal and S. Pandit, *Numerical simulation of unsteady squeezing nanofluid and heat flow between two parallel plates using wavelets*, Int. J. Therm. Sci., *118* (2017), 410–422.
[26] A. T. Moltot, E. H. Gorfie, G. A. Zergaw, and H. Dessie, *Unsteady MHD flow of tangent hyperbolic ternary hybrid nanofluid in a darcy-forchheimer porous medium over a permeable stretching sheet with variable thermal conductivity*, F1000Res., *14* (2025), 152.
[27] M. Nasir, M. Waqas, O. A. Bég, N. Zamri, H. J. Leonard, and K. Guedri, *Dynamics of tangent-hyperbolic nanoliquids configured by stratified extending surface: Effects of transpiration, Robin conditions and dual stratifications*, Int. Commun. Heat Mass Transf., *139* (2022), 106372.
[28] A. M. Obalalu, O. A. Olayemi, C. B. Odetunde, and O. A. Ajala, *Significance of thermophoresis and Brownian motion on a reactive Casson-Williamson nanofluid past a vertical moving cylinder*, Comput. Therm. Sci., *15* (2023).
[29] S. Pandit and S. Sharma, *On the use of wavelets for analysis of nanofluid flow and thermal transmission through asymmetric porous channel*, Proc. Natl. Acad. Sci. India A, *92* (2022), 571–583.
[30] A. M. E. I. Shafey, F. M. Alharbi, A. Javed, N. Abbas, H. A. ALrafai, S. Nadeem, and A. Issakhov, *Theoretical analysis of Brownian and thermophoresis motion effects for Newtonian fluid flow over nonlinear stretching cylinder*, Case Stud. Therm. Eng., *28* (2021), 101369.
[31] I. Waini, F. N. Jamrus, A. R. M. Kasim, A. Ishak, and I. Pop, *Homogeneous-heterogeneous reactions on Al_2O_3-Cu hybrid nanofluid flow over a shrinking sheet*, J. Adv. Res. Fluid Mech. Therm. Sci., *102* (2023), 85–97.